Hall A Status Report - 2003

Insert picture here

Edited by Kathy McCormick, David Armstrong and Kees de Jager
December 2003

Contents

1 Introduction **9**

2 Standard Hall A Facilities **10**
2.1 BigBite Spectrometer 10
2.2 Septum Magnets 13
2.2.1 Overview 13
2.2.2 Developments in 2003 13
2.3 Møller Polarimeter 15
2.4 The Hall A Compton Polarimeter 16
2.4.1 Overview 16
2.4.2 Helicity Timing 16
2.4.3 Detectors 16
2.4.4 Data Acquisition 18
2.4.5 Control Software 21
2.4.6 Recent Data 21
2.4.7 Upgrade Plan 21
2.5 Polarized ^{3}He Target 23

3 General Hall Developments **25**
3.1 Detector Developments 25
3.1.1 The E02-013 (G_E^n) Experimental Setup 25
3.1.2 Detectors for E00-110 (DVCS) and E03-106 (nDVCS) . . . 29
3.2 Preparations for Hall A Parity-Violation Experiments 32
3.2.1 Polarized Source Development for Hall A PV Experiments . 32
3.2.2 Data Acquisition and Analysis 35
3.2.3 Detector and Beam Monitors 37
3.3 The Hall A RICH Detector 39
3.3.1 Introduction 39
3.3.2 Cosmic Test and System Improvements 39
3.3.3 Conclusions 41
3.4 High Resolution Trigger Counter S2m 42
3.4.1 Signal Processing 42
3.4.2 Results 42
3.5 New Raster with No Dwell 44
3.6 Offline Analysis Software 45
3.6.1 The C++ Analyzer 45
3.6.2 ESPACE 49
3.7 DAQ in Single Arm Mode 51

4 Summaries of Experimental Activities **53**
4.1 E89-044 53
4.2 E91-011 56
4.3 E93-050 60
4.4 E97-103 62
4.5 E97-110 65
4.6 E97-111 69
4.7 E98-108 72
4.8 E99-114 75
4.9 E00-007 78
4.10 E00-102 79
4.11 E01-001 82

5 References **86**

6 Hall A Collaboration Member List **89**

7 Publications **95**

8 Theses **97**

List of Figures

1 CAD drawing of the BigBite auxiliary plane. 11
2 Photo of the auxiliary plane during its construction. 11
3 CAD drawing of the BigBite trigger plane. 12
4 Photo of the trigger plane during its construction. 12
5 Shown is a CAD drawing of how the short-range correlation experiment will look, once it is installed in Hall A. Located left of center is the new scattering chamber which will match BigBite's large out-of-plane acceptance. The stand for the spectrometer mounts under the target platform and to a curved track located on the floor. The BigBite dipole magnet is shown in yellow and blue. Behind the magnet are the auxiliary and trigger planes. Behind the CAD person is a neutron detector which will also be used during the experiment. 12
6 Helicity Pair-Sync (PS) signal (bottom trace) added to the G0 helicity scheme for compatibility with the Compton Polarimeter. . . 17
7 Singles rates in the four planes of the electron detector as a function of micro-strip number. 19
8 Coincidence rates in the four planes of the electron detector as a function of micro-strip number. 20
9 Preliminary beam polarization measurement performed at 2.8 GeV between June 31 and August 05, 2003. Blue points are results of the coincidence analysis, red points are electron only. Only statistical errors are presented. 22
10 Preliminary layout of the G_E^n neutron detector. The electronics schematic is also shown. 26
11 The control of the charge asymmetry and the convergence of the average charge asymmetry during a run from tests in June, 2002 demonstrate the effectiveness of feedback using the IA cell. 34
12 Time dependence of the charge asymmetry across the 33 ms helicity-flipping window. 36
13 The charge asymmetry distribution displays multiple peaks caused by the history of pair ordering in previous pairs. 36
14 The two-segment HAPPEX detector. 38
15 Distribution of the number of photo-electrons and of the charge per cluster for the cosmic tests in August 2003. The MWPC was operated at 2150 V with pure methane. The average number of photo-electrons per ring was 10.6. 40
16 Distribution of the number of photo-electrons and of the charge per cluster for the cosmic tests in November 2003. The MWPC was operated at 2120 V with pure methane. The average number of photo-electrons per ring was 13.4. 40

17 The event display for a single cosmic trigger. The large cluster in the middle is the signal from a MIP, the clusters around it are from the Cherenkov light. 41
18 The fully assembled S2m scintillator plane. 42
19 S2m Time-difference resolution. 43
20 Results for the reconstructed target quantities δ (momentum), y (in-plane position), θ (out-of-plane angle), and ϕ (in-plane angle). The data are from an optics study that used a 9-foil carbon target and the sieve slit collimator on the left HRS (see text). In each panel, black histograms represent results from the C++ analyzer, and red (lighter colored) histograms were obtained with ESPACE. Since the results are nearly identical, the two histograms are almost indistinguishable. 47
21 Histograms of the event-by-event differences of the target variables reconstructed by the C++ analyzer and by ESPACE. The data are the same as in Fig. 20. The widths of the distributions are about an order of magnitude smaller than the measured spectrometer resolutions for each variable. 48
22 Example of a good track in the HRS visualized by the prototype event display of the C++ analyzer. Wire chamber clusters as well as active scintillator paddles and shower blocks are shown. The track is drawn using the reconstructed focal plane coordinates from the VDC. 50
23 Sample of the 3-body break-up data [22] for several recoil momenta. Theoretical calculations are shown for different approximations of the (e,e′p) reaction process. The green dashed line indicates the expected position of the maximum of the cross section assuming a correlated pair in the nucleus. 53
24 Very high recoil momentum distribution in ^{3}He; triangle and dot symbols are ^{3}He(e,e′p)d analysis results [21] and the star symbol of the last point is the reconstructed cross section from the ^{3}He(e,e′d)p measurement. 54
25 Data for response functions at $W = 1.22 \pm 0.02$ GeV and $Q^2 = 0.9 \pm 0.1$ (GeV/c)^2 are compared with Legendre fits in the *sp* truncation (dashed) and with a few extra terms as needed (solid). Results from CLAS are shown as green squares for $k_i = 1.645$ GeV or blue open circles for $k_i = 2.445$ GeV. 56
26 Data for response functions at $W = 1.22 \pm 0.02$ GeV and $Q^2 = 0.9 \pm 0.1$ (GeV/c)^2 are compared with fits that vary *sp* (dashed) versus *spd* (solid) multipole amplitudes. Results from CLAS are shown as green squares for $k_i = 1.645$ GeV or blue open circles for $k_i = 2.445$ GeV. 58

27 EMR and SMR data for $Q^2 = 0.3$ (GeV/c)^2 are compared with MAID2000 (solid), DMT (dashed), and SAID (dash-dot). In addition, the red star shows the result for $W = 1.23 \pm 0.02$ GeV, $Q^2 = 1.0 \pm 0.2$ (GeV/c)^2. Left: results from truncated Legendre expansion. Right: results from multipole analysis varying sp amplitudes w.r.t. MAID2000. Within each panel data and curves employ the same formulas. 59
28 Cross section ratio $H(e,e'p)\gamma/H(e,e'p)\pi^0$, at $Q^2 = 1.0$ GeV^2 in a bin $\cos\theta_{\gamma p}^{CM} > 0.95$, where $\theta_{\gamma p}^{CM}$ is the angle between the recoil proton and the virtual photon q in the photon-proton Center-of-Mass frame. 61
29 Comparison of $Q^2 = 1$ GeV^2 virtual compton scattering cross sections ($\bullet$) at $\theta_{\gamma\gamma}^{CM} = 167^\circ$ and real compton scattering data at $\theta_{\gamma\gamma}^{CM} = 159 - 160^\circ$ [34] ($\star$) $128 - 132^\circ$ [32] ($\diamond$), 141° [33] ($\triangle$), $130 - 132^\circ$ [35] ($\circ$), 131° [36] ($\Box$), $128 - 105^\circ$ [52] ($\times$). The solid curve is a s^{-6} scaling function normalized to the second Cornell point. The dashed curve is the Bethe-Heitler + Born cross section including the t-channel π^0 exchange diagram. The dotted curve is the Bethe-Heitler alone. 61
30 Preliminary results for g_2^n from E97-103. Errors are statistical with systematic errors shown by the solid band. Also shown are calculations of g_2^{ww} using the Blumlein and Bottcher NLO fit to world data on g_1. 63
31 Kinematical coverage of the experiment. 66
32 Elastic asymmetry online results for run 1. 67
33 Elastic asymmetry online results for run 2. 67
34 Optics data from run 2 68
35 Q^2-position of the expected results with their uncertainty 68
36 Preliminary results for the reduced cross sections at a beam energy of 3170 MeV. The error bars only show the statistical uncertainty. The dashed line (short dashes) shows the theoretical prediction by Laget in PWIA, the solid line depicts the full calculation, the dotted line only includes FSI. The dashed curve (long dashes) is a Glauber calculation by Ciofi and Morita, the dash-dotted curve additionally includes finite formation time effects. 70
37 The online missing mass yield taken in March 2002 at $Q^2 = 1.9$ (GeV/c)^2, $W = 1.95$ GeV and $t = t_{min}$. 72
38 The longitudinal (upper) and transverse (lower) response function at Q^2- 2.35 GeV/c^2 for $H(e,e'K^+)$ as a function of the invariant 4-momentum, t. 73

39 Shown are ratios of the longitudinal to transverse responses as a function of Q^2 from the previous E93-018 and from this experiment. 74
40 Preliminary $H(\gamma,\gamma p)$ cross sections, divided by the elementary Klein-Nishina cross section, as a function of the invariant momentum transfer t. 76
41 Preliminary fixed-angle scaling exponent (Eq. 5). The Cornell data are from [52]. The curve from A. Radyushkin is a prediction of the handbag hypothesis. 76
42 Projected A_{LT} data compared to E89-003 results and calculations of Udias *et al.* Open circles are anticipated data points from E00-102, solid squares are E89-003 data obtained at slightly different kinematics. 80
43 E00-102 kinematics. LHRS remained fixed at 12.5° throughout the experiment while RHRS varied around the direction of parallel kinematics. 80
44 The (Q^2,ε) points at which proton spectra were taken. The lines are fixed values of beam energy: 1.912 (red), 2.262 (black), 2.842 (green), 3.772 (blue), and 4.702 GeV (magenta). The $Q^2 = 0.50$ GeV^2 points served to monitor the luminosity. 82
45 Missing momentum spectrum (in MeV) at $E_{beam} = 2.262$ GeV, $\theta_p = 12.526°$ ($Q^2 = 3.20$ GeV^2, $\varepsilon = 0.131$). The data from the LH2 target is shown in black, while the total simulated spectrum is in red. The spectrum is decomposed into contributions from the elastic peak (blue), protons from the $\gamma+p \to \pi^0+p$ reaction (green) and protons coming from the solid endcaps of the target (magenta). 83
46 Reduced cross sections plotted as a function of ε. The solid line is the best linear fit to the data and the dotted line is the best fit with the slope fixed to match the results of the polarization transfer experiments [58,59]. 85

List of Tables

1 DAQ Deadtime in Single Arm Mode 51
2 The left-arm detector stack used in the experiment. 78

1 Introduction

The year 2003 has been both a challenging one and a productive one for the Hall A collaboration. Challenges included the several schedule shifts due to delays with the delivery of the septum magnets, the discovery during a running experiment that the first septum had been delivered to us by the vendor mis-wired, and the additional schedule delay due to the consequences of Hurricane Isabel. Despite these challenges, the year was a fruitful one, whether measured in terms of refereed publications appearing or being accepted for publication, talks and conference proceedings, PhD theses produced, or detector developments for upcoming experiments.

After experiments E00-007 (Gilman, Holt, Meziani) and E01-020 (Boeglin, Jones, Klein, Ulmer, Voutier) were completed in October and November of 2002, the Hall A was down for the installation of the polarized ^{3}He target. Starting in early January 2003 the measurement of spin-duality in ^{3}He (E01-012: Chen, Choi, Liyanage) successfully took data. After the run was completed, the first of the two septa magnets was installed, and the polarized ^{3}He target was moved 80 cm upstream to the septum interaction point. The small-angle GDH experiment then began (E97-110: Chen, Deur, Garibaldi) data-taking in late April. It was quickly discovered that the septum magnet was mis-wired, and was not functioning as a dipole. Despite this, the experiment was able to take useful data under these conditions during the first stage (April-May) of the run. The septum was then re-wired in June, and the second stage of the experiment successfully took data in July and August. Since then, the hall has been down for the installation of the second septum and the removal of the polarized ^{3}He target, and for the recovery from the hurricane.

The schedule for the near future for Hall A includes commissioning of the second septum magnet in December, followed by E94-107, High Resolution Hypernuclear Spectroscopy in the 1-p shell (Frullani, Garibaldi, LeRose, Markowitz, Hashimoto) which will start early in January 2004. The delivery of beam with the very small energy spread required for this experiment in parallel with the high space-charge beam for the G0 experiment, which is scheduled to run simultaneously in Hall C, will be a significant challenge for accelerator operations. Following the Hypernuclear experiment will be a return to HAPPEx parity violation experiments; a short initial run on the HAPPEx-He (E00-114: Armstrong, Michaels) in mid-April followed immediately by the majority of running for HAPPEx-II (E99-115: Kumar, Lhuillier) on hydrogen, which will continue until late June. After these experiments comes the installation of the Deeply Virtual Compton Scattering (DVCS) experiments (E00-110: Bertin, Hyde-Wright, Ransome, Sabatie and E03-106: Sabatie, Bertin, Hyde-Wright, Voutier) which should commence data-taking in mid-August, and will continue through the end of FY04. Following this,

the first installation of the BigBite spectrometer will commence.

2 Standard Hall A Facilities

2.1 BigBite Spectrometer

Contributed by D.W. Higinbotham

Six approved Hall A experiments require the BigBite spectrometer [1–6]. This spectrometer consists of a single large dipole magnet and a detector package. In its most standard configuration, the spectrometer will have a solid angle acceptance of 96 msr with a vertical acceptance of ±300 mrad and a horizontal acceptance of ±80 mrad. The momentum acceptance of the spectrometer is nearly unlimited, though the momentum resolution, dp/p, and acceptance decrease appreciably for momenta greater than 1 GeV/c. The spectrometer will have an extended target capacity of ±10 cm at 90°. In general, the BigBite spectrometer will be a very flexible, large acceptance device which can easily be reconfigured for different experiments. For the six approved experiments there are already three different detector packages being built.

The first package, which is for the short-range correlation experiment [1], has already been constructed and is presently located in the Jefferson Lab Test Lab building. This package is comprised solely of scintillator planes. The first plane, known as the auxiliary plane, will be located immediately after the BigBite magnet and is shown in Figs. 1 and 2. A segmented trigger plane, which will be located 1 m further back, is shown in Figs. 3 and 4. The trigger plane is comprised of 3 mm and 30 mm scintillating layers to provide dE/E particle identification and will have a timing resolution better than 0.5 ns. The auxiliary and trigger planes together will provide ∼5% momentum resolution at 300 MeV/c with ∼10 mrad angular resolution. The auxiliary plane has one-sided read-out, so the spectrometer in this configuration will not be able to determine the reaction vertex by itself. In Fig. 5 the BigBite spectrometer is shown as it will look during the short-range correlation experiment.

The second detector package, optimized for detecting low-energy hadrons, will use the same trigger plane but the auxiliary plane will be replaced by two drift chambers. The chambers will allow BigBite to provide ∼1% momentum resolution, ∼3 mrad angular resolution in θ and ϕ, and 3 mm y-target resolution. This package will be used for measurements of threshold pion production [2], threshold deuteron electrodisintigration [4], and detailed measurements of the ^{3}He system [5].

The third detector package is being optimized for detecting high energy electrons and will be used for the G_n^E and transversity experiments [3,6]. This package will use three drift chambers to give the spectrometer multi-track capabilities. In addition, this package will have a shower calorimeter. Further details of this system can be found in the G_n^E section.

The dipole magnet for the BigBite spectrometer is already in the Hall and its power supply has been tested. The stand for the BigBite magnet and a carriage for the various detector packages has been designed and most of the components are already in the Hall. In addition to being used for the BigBite experiments, the DVCS collaboration will use the BigBite stand for mounting their experiment. Parts of the stand and detector carriage can seen in Fig. 5.

Many groups have already built or are building various parts for the BigBite spectrometer. Eli Piasetzky and the Tel Aviv group have built the auxiliary scintillator plane. John Annand and the Glasgow group have built the trigger plane. For experiments which require a cryotarget, Richard Lindgren and the University of Virginia have committed to building a new scattering chamber, which will have a higher opening to match the large out-of-plane acceptance of the BigBite spectrometer. Nilanga Liyanage and the University of Virginia are building the wire chambers. The G_n^E collaboration is constructing the shower calorimeter and is working on building a polarized ^{3}He target for use with the BigBite spectrometer. William Bertozzi and the M.I.T. Nuclear Interaction Group have taken charge of building and testing the BigBite data-acquisition system. In addition to the groups mentioned above, many members of the BigBite working group have helped build and test the various systems and Jefferson Lab has done the majority of the design work.

The first BigBite experiment, the short-range correlation experiment, is on the Jefferson Lab tentative schedule for late 2004 and the second BigBite experiment is expected to be the G_E^n experiment and will be ready to run by the middle of

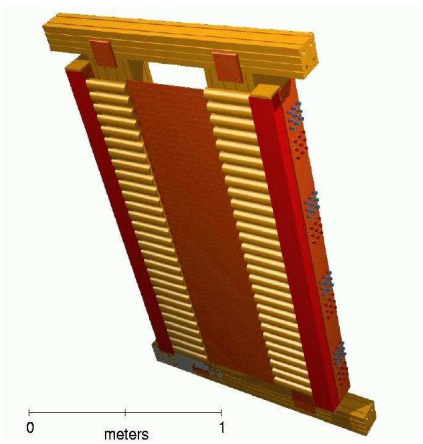

Figure 1: CAD drawing of the BigBite auxiliary plane.

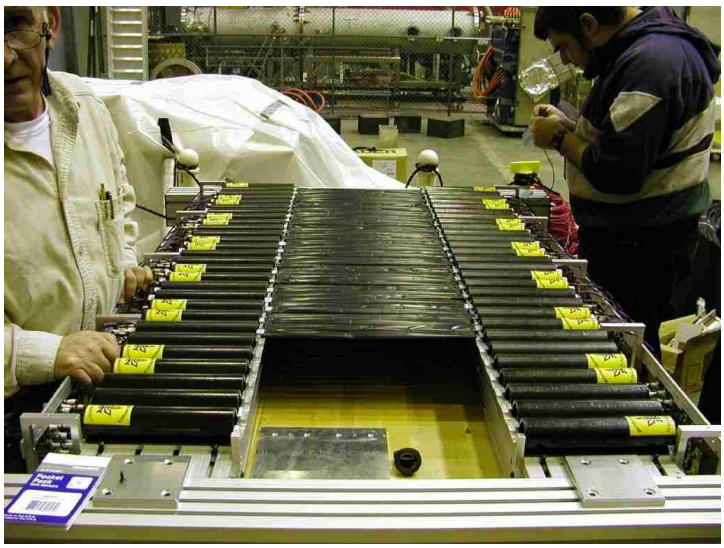

Figure 2: Photo of the auxiliary plane during its construction.

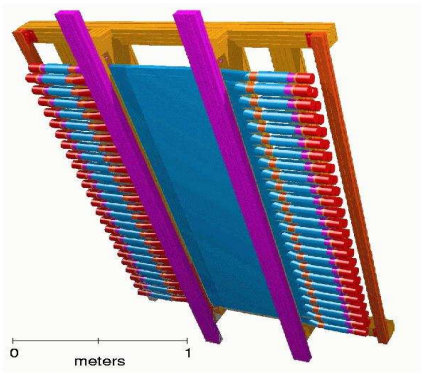

Figure 3: CAD drawing of the BigBite trigger plane.

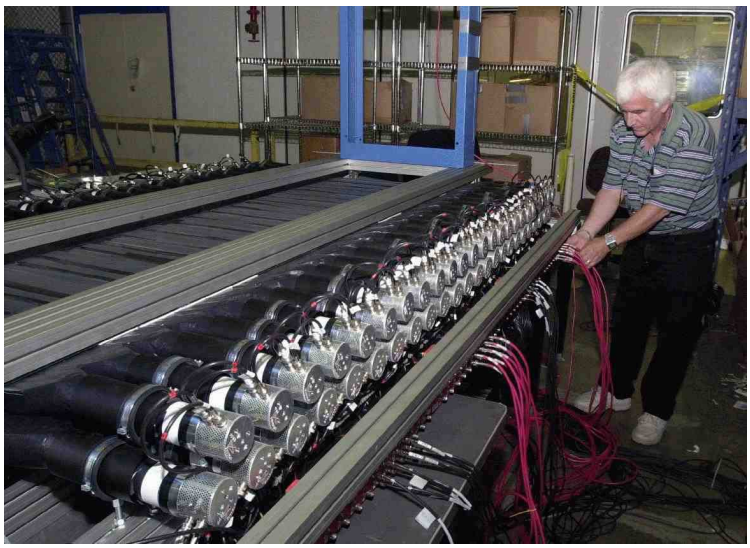

Figure 4: Photo of the trigger plane during its construction.

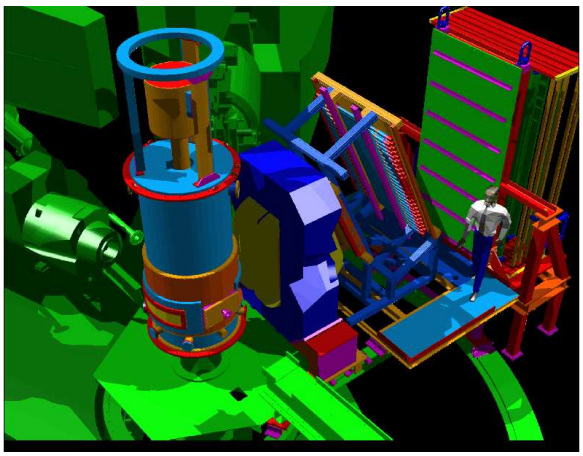

Figure 5: Shown is a CAD drawing of how the short-range correlation experiment will look, once it is installed in Hall A. Located left of center is the new scattering chamber which will match BigBite's large out-of-plane acceptance. The stand for the spectrometer mounts under the target platform and to a curved track located on the floor. The BigBite dipole magnet is shown in yellow and blue. Behind the magnet are the auxiliary and trigger planes. Behind the CAD person is a neutron detector which will also be used during the experiment.

2005.

2.2 Septum Magnets

Contributed by J.J. LeRose

2.2.1 Overview

The two septum magnets (left and right) were manufactured by BWXT Technologies of Lynchburg Virginia under contract with INFN Rome. They were designed to allow access to scattering angles from 6 to 12.5° up to the maximum momentum of each spectrometer with no degradation in the optical properties of either spectrometer (except for some reduction in solid angle acceptance).

2.2.2 Developments in 2003

2003 saw much progress with the implementation of the septum magnets in Hall A. The first septum, the right one, arrived at Jlab in January and was installed in the Hall in March. The magnet had two serious problems, a heat leak between the warm bore and the cold mass, and the upper and lower coils were wired with opposite polarities (so-called "bucked" coils). The warm bore heat leak problem was temporarily solved by installing a cooling system in the magnet bore to reduce the temperature in the bore to the point (-100 degrees C) where the coils could be cooled sufficiently to go superconducting. Unfortunately, this limited access to the magnet bore making direct measurement of the magnetic field difficult. Consequently, it was not until well into commissioning that the "bucked" coil problem was identified. Nevertheless, preliminary data were taken for the Small Angle GDH experiment (E97-110). After a very difficult data taking effort in April and May the right septum was warmed to room temperature and its cryostat was opened allowing access to the inter coil splices. At that time the incorrect wiring was corrected and verified by field measurements. Subsequently, the right septum was used again for the second run of E97-110 in both the 6 and 9° configurations. This time the optics looked much better; having the correct magnetic field makes all the difference. Good reconstruction of the sieve hole pattern was possible without any optimization of the previoulsy calculated optics database. To date the right septum has achieved a maximum current of 438 Amps, exceeding the requirements for HAPPEX II (3.1 GeV/c at 9°).

After E97-110 finished running in August the second septum (left) was delivered. It included design modifications (added heat sinks on the coil, new redesigned shield, slightly smaller bore tube with better insulation) to improve coil cooling in general and eliminate the warm bore heat leak. At that time the right septum was partially disassembled in order to incorporate these same modifications. At the time of this writing (December 5, 2003) both septum magnets are installed on the pivot in the Hall at 6° and are cooling down in preparation for the Hypernuclear Spectroscopy Experiment (E94-107). After some preliminary

adjustments in the cryogenic feed system, the left septum has achieved coil temperatures of 5.95 K(5.90 K) in the lower(upper) coil and 4.8 K in the yoke (colder than ever previously achieved in the right septum) and reached 197 A in its first serious training run. This is comparable to the first training run with the right septum and already exceeds the current needed for E94-107. Moreover, recovery time from the first training quench was much shorter (on the order of 1-2 hours) than previously seen with the right septum (about 6 hours). The right septum is cold but the cryogenic flow has not yet been turned up enough to reach superconducting temperatures. Neither magnet shows any sign of having the previously observed warm bore heat leak (**i.e.** the bore stays warm).

2.3 Møller Polarimeter

Contributed by Eugene Chudakov

The Hall A beam line is equipped with a Møller polarimeter, whose purpose is to measure the polarization of the electron beam delivered to the hall. During the period from Dec. 1, 2002 to Dec. 1, 2003, 25 measurements of the beam polarization have been made.

The systematic error of each measurement is estimated to be about 3% relative, while the statistical error is about 0.3%.

The systematic error is dominated by the error on the target polarization. We are trying to reduce this error. The target is a magnetized ferromagnetic foil and its electron polarization is measured by measuring the foil magnetization. There was a gradual improvement of the magnetization measurements during the last year, however we found a relatively strong variation of the magnetization results along the foil. In order to treat these variations correctly we can measure the relative foil polarization across the foil, using the electron beam. For that, a new target chamber is being manufactured, which would provide the motion of the target across the beam, in two projections.

An ambitious project is under consideration, to use polarized atomic hydrogen gas for the target. Such a target of 100% polarized electrons could reduce the polarimetry systematic error to about 0.5%. Detailed feasibility studies have been made [7] and no serious problem has been identified so far.

2.4 The Hall A Compton Polarimeter

Contributed by Sirish Nanda and David Lhuillier

2.4.1 Overview

The Hall A Compton polarimeter has been in operation during most of the running time in the Hall this year. Continuous measurements of beam polarization during acceptable beam conditions for the spin duality (E01-012) and the GDH sum rule (E97-110) experiments have been carried out successfully this year. The primary limitation to the operation of the polarimeter has been due to unacceptable backgrounds in the Compton detectors arising from beam halo during simultaneous beams in Halls A and C.

During the year, the Compton polarimeter configuration has seen substantial upgrades in its hardware as well as software, improving overall performance and reliability of the system. In the following sections, developments in the Compton Polarimeter, results from recent experiments, and future plans are presented. Generally, the polarimeter performed reasonably well down to a beam energy of 2.5 GeV.

2.4.2 Helicity Timing

In order to handle counting rates as high as 100 kHz, the Compton data acquisition design relied on the 15 Hz toggle signal to flip-flop between two acquisition processors for consecutive helicity states. The introduction of the new helicity timing scheme for the G0 Experiment posed a challenge for the running of the Compton polarimeter data acquisition. In going from pseudo-random pairs of helicity assignments to quartets, the G0 scheme replaced the old 15 Hz pair signal with the quartet (QRT) signal shown in Fig. 6. Following discussions with the G0 group, it was decided that a pair-sync (PS) signal would be implemented to the G0 timing generator module to maintain compatibility with the Compton polarimeter. The PS signal (shown in Fig. 6) was delivered to Hall A at 14.8 Hz by January 2003 and the Compton polarimeter was tested successfully with the new signal, in both normal and delayed reporting modes.

2.4.3 Detectors

In order to extend the dynamic range of the Compton polarimeter to lower energies, last summer the electron detector was opened to bring the micro-strips closer to the primary beam. A 200 μm aluminum foil was also installed in front of the first of the four micro-strip planes to shield it against the synchrotron radiation emitted in the third dipole of the chicane. The detector was operated successfully during the GDH experiment only 3 mm away from the beam centroid with a minor

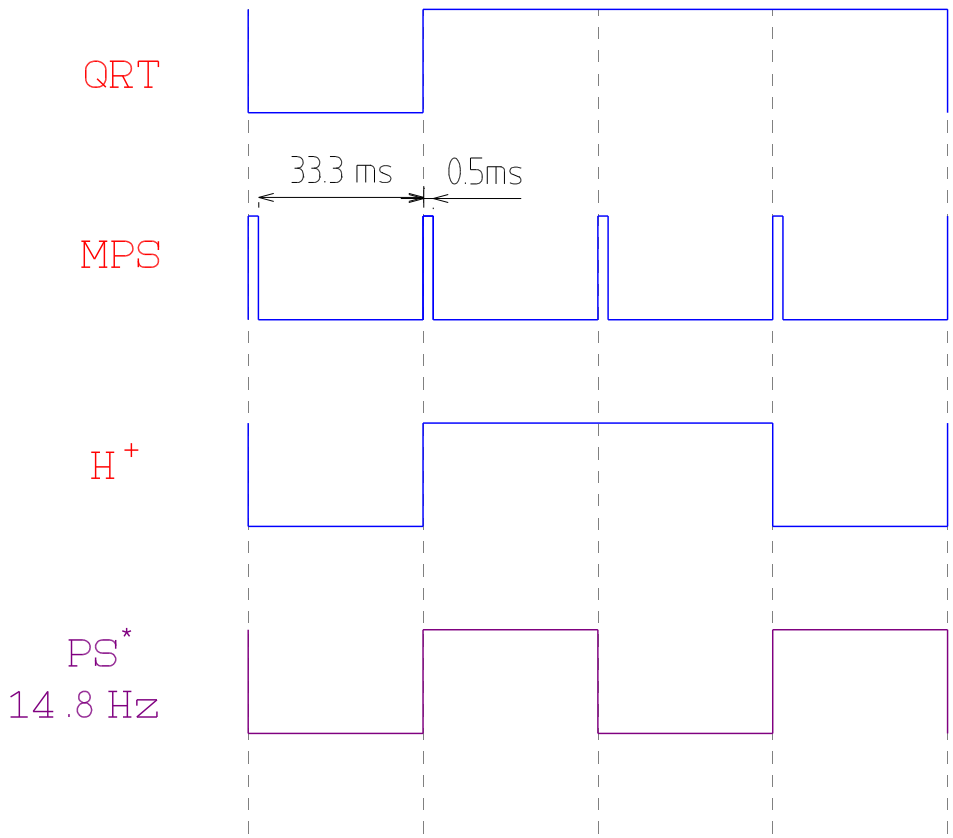

Figure 6: Helicity Pair-Sync (PS) signal (bottom trace) added to the G0 helicity scheme for compatibility with the Compton Polarimeter.

upgrade of the tuning procedure of the Compton chicane. As shown in Fig. 7 the four planes are now working.

A beam halo, characterized by its exponential shape, has been measured typically 10 times higher than the Compton rate at 3mm and comparable to the Compton rate at 7mm. This background is totally removed when requiring a coincidence with the photon detector in the trigger (Fig. 8). A possible origin of this halo could be the continuous offset of the diode laser at the source as a result of which it doesn't turn off completely between two beam pulses. The data collected show that if the beam halo can be reduced, operating the electron detector that close to the primary beam would allow accurate measurements, based on the semi-integrated method [8], down to 2.5 GeV.

In addition, a new set of four planes of silicon micro-strip detectors have been procured from Canberra Systems. They have been tested and mounted on a high precision frame. The new assembly servers as a spare electron detector.

2.4.4 Data Acquisition

The data-acquisition and analysis packages for the Compton polarimeter have been integrated into a single Linux platform which provides more efficient handling of Compton data. The new machine, named compton.jlab.org, is a modern dual processor Pentium server, running RedHat Linux 7.3.

In the earlier system, a Sun machine, adaqs1, was used for data acquisition, on-line monitoring of events, and EPICS control of the hardware. This machine, approaching obsolescence, has been problematic recently. The off-line analysis was carried out in an older PC, adaqcp, with poor performance. Typical analysis times exceeded acquisition times by a factor 1.5, even at modest beam currents of 10 μA generally used in the ^{3}He polarized target experiments. Hence, in a continuous running scenario, the results of the Compton polarimeter were not readily available.

The original acquisition software developed by CEA (Saclay) was specific to SunOS. It relied on a non-standard version of CODA, with the DD event monitoring system, that is no longer supported by Jefferson Lab. Migration of the acquisition software to Linux was, hence, a major project requiring significant development effort. The task was carried out by the Compton group and the CODA group in consultation with Damien Neyret of Saclay. David Abbott of the CODA group developed the CODA source tree for the RedHat Linux 7.3 system. Carl Timmer of the CODA group developed the crucial TCL application interface to the ET event monitoring system. Additional effort went into incorporating MySQL database support in CODA. With these developments incorporated into CODA and tested in the Compton set up, the CODA group has now released the new version as CODA 2.2.5.

Furthermore, the data analysis software has been upgraded to ROOT based programs from the original PAW based system. Several improvements have been

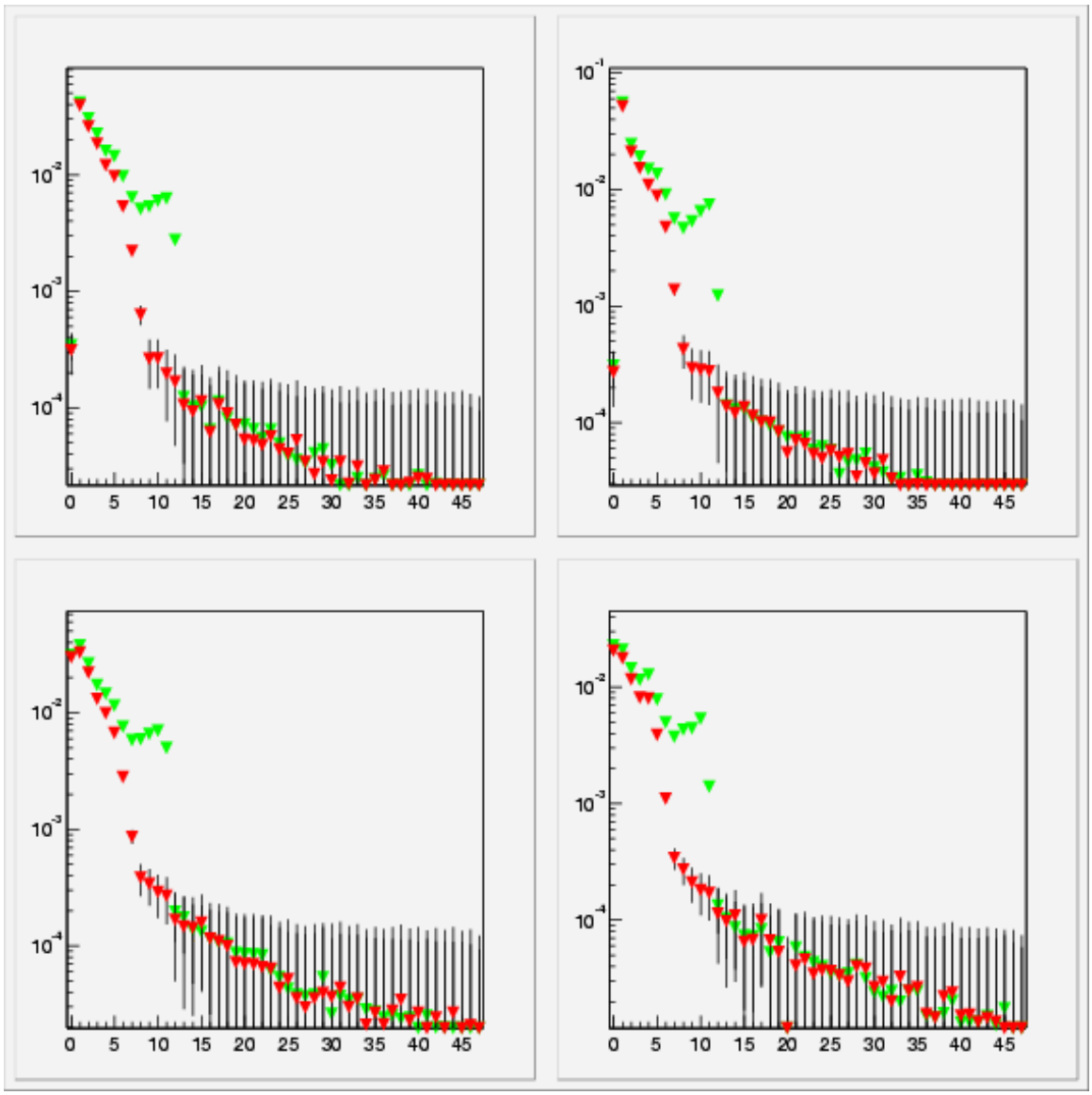

Figure 7: Singles rates in the four planes of the electron detector as a function of micro-strip number.

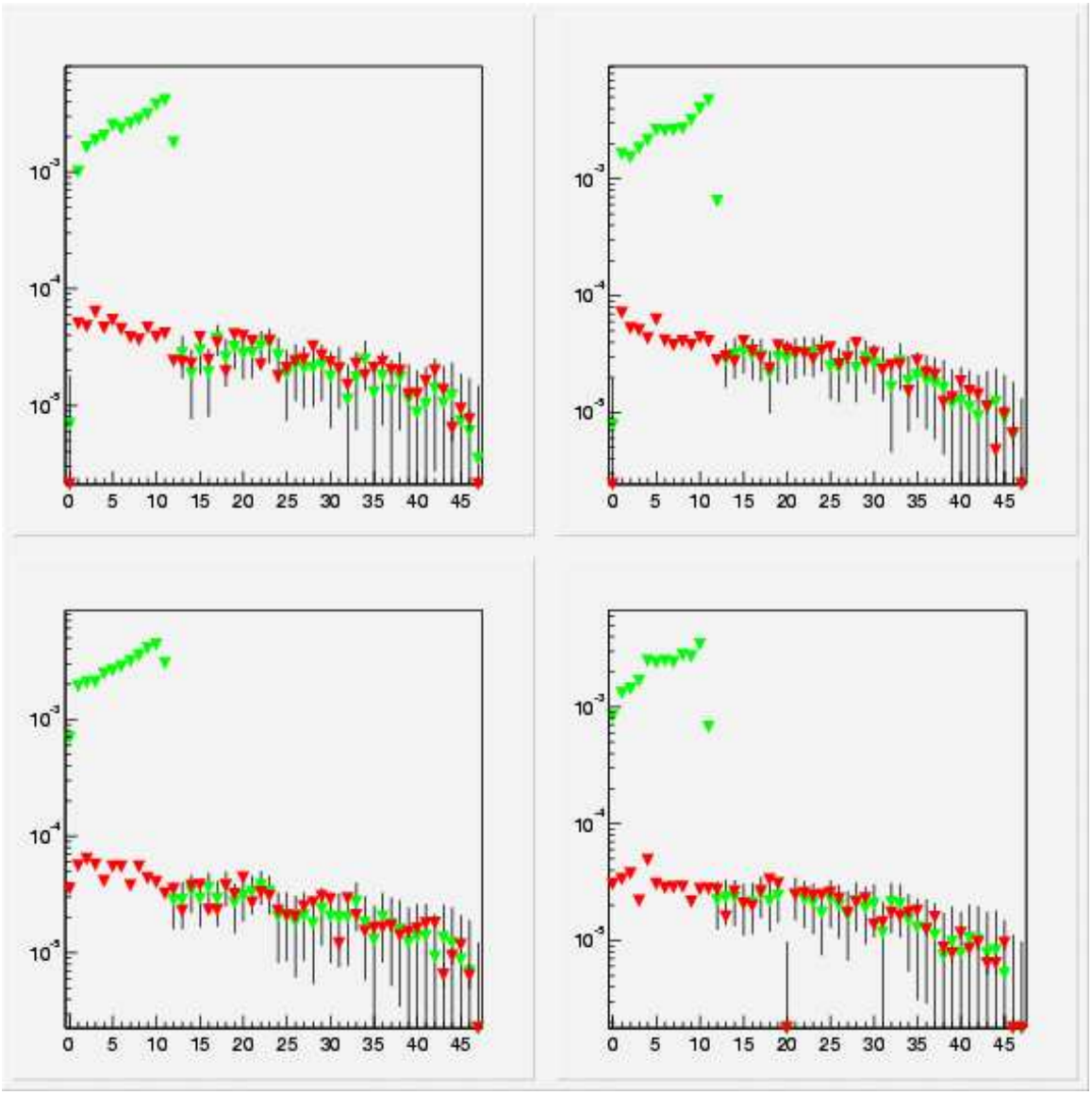

Figure 8: Coincidence rates in the four planes of the electron detector as a function of micro-strip number.

made to the software package eventSelection, the main analysis engine, to analyze coincidence data more reliably. The package has been ported to the new Compton machine. The analyzer is capable of analyzing electron-only or electron-photon coincidence data.

With the performance upgrades, the new system has reduced the analysis time to 0.1 of the acquisition time, facilitating quasi-online polarization results.

2.4.5 Control Software

A process of migration of the EPICS control software, originally developed by the Saclay group, to the Jefferson Lab EPICS software group was launched this year. We envision a phased transition of the package until it is fully taken over by the EPICS group. A second single-board computer, serving as a slave IOC for this development, has been installed in the Compton controls VME crate to facilitate the porting process. The new IOC uses the common server for Hall A managed by the EPICS group.

The first phase of the migration, namely control of the electron detector, has been successfully implemented and tested.

2.4.6 Recent Data

Compton polarimeter data taken for the GDH experiment between June 31 and August 05, 2003 have been analyzed for both electron only and electron-photon coincidence triggers. Figure 9 shows preliminary results obtained at 2.8 GeV. The two methods are in good agreement although they have different systematic errors.

2.4.7 Upgrade Plan

We are presently developing a conceptual design to upgrade the present Hall A Compton polarimeter by doubling the laser frequency with commercially available components. The upgrade is motivated by upcoming high accuracy experiments with very demanding requirement on the beam polarization accuracy. The requirement of the Lead Parity experiment, for example, is on the order of 1% relative accuracy at 0.85 GeV.

Defining k the photon energy and E the electron beam energy, the figure of merit of a Compton measurement scales with $k^2 \times E^2$, making high accuracy polarimetry a real challenge at low energy. The present infra-red system, while capable of achieving such accuracies at higher energy ($\geq$ 6 GeV), falls far short at lower energies. We plan to upgrade the existing Fabry-Perot cavity operating at 1064 nm (IR) with about 1.5 kW power to a 532 nm (green) cavity with the same power. Doubling the frequency, the figure of merit will increase 4 times compared to the IR system, for the same photon density in the cavity. In addition, improvements to the electron detector and photon calorimeter combined with the

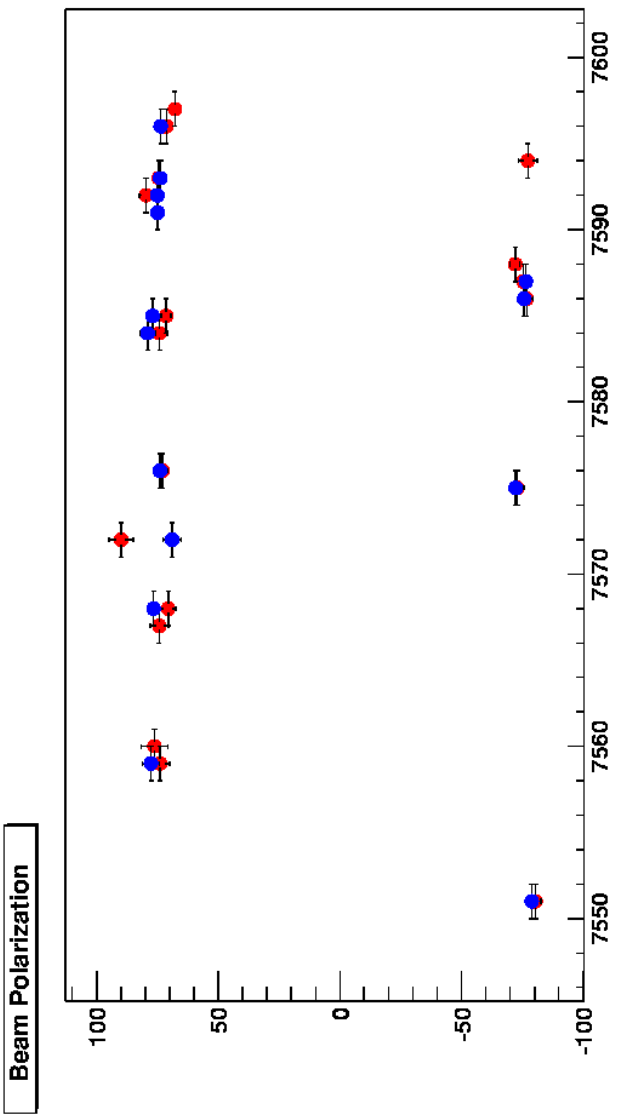

Figure 9: Preliminary beam polarization measurement performed at 2.8 GeV between June 31 and August 05, 2003. Blue points are results of the coincidence analysis, red points are electron only. Only statistical errors are presented.

development of a new integrated method shows promise of an absolute accuracy well below 2% at 0.85 GeV beam energy.

2.5 Polarized ^{3}He Target

Contributed by Jian-Ping Chen

The Hall A polarized ^{3}He target [9] was first used successfully for experiments E94-010 [10] and E95-001 [11] in 1998-1999, then E99-117 [12] and E97-103 [13] in the summer of 2001. In January-February 2003, it was used for E01-012 (Spin-Duality) [14]. After modification for small-angle capability, it was then used for E97-110 (Small Angle GDH) [15] in April-May and July-August.

The target was used in its standard configuration for the Spin-Duality experiment. One target cell ruptured after 4 weeks of running at 10 μA beam current, which is the usual radiation level for rupture. The second cell lasted to the end of the experiment. There was significant depolarization due to the 'masing' effect. By applying additional field gradients, the masing effect was minimized. The average in-beam target polarization during the experiment was about 37%. In addition to the masing effect, another problem also contributed to the average target polarization falling below 40%. At the beginning of the experiment, half-wave plates in the laser beam lines were set in the wrong orientation such that in the 180° field configuration the optical pumping was not in effect. It caused significant polarization losses, but was discovered quickly and corrected.

The main modification for the Small Angle GDH experiment was that the target cell changed from cylindrical to ice-cream-cone shaped to minimize the material thickness in the path of the scattered particles. With intensive effort from the glass blowers at Princeton and UVa, and from both polarized ^{3}He target groups at UVa and William and Mary, over twenty cells were produced. Two of these cells were tested to have excellent lifetimes (over 50 hours) and high polarizations (over 40%), and a few more were tested to be acceptable (maximum polarization above 30%). The best target cell was used for the whole period (about 3 weeks in April-May) of the first running period for E97-110. During the second running period (July-August) only standard-shaped cells were used. The first cell ruptured after only one week in beam. In contrast to the usual rupture pattern where the rupture happens in the pumping chamber after 3-4 weeks of continuous high current beam, this rupture happened in the target chamber. The cause could not be determined for certain. It was probably related to beam heating and insufficient cooling might have contributed. We increased the cooling flow rate and raster size to be safe. The second target cell lasted to the end of running (one month) without rupture under the new condition.

The Septum magnet used in the Small Angle GDH experiment introduced a non-negligible field gradient at the target region. Compensation coils in the vertical direction (y) were built to minimize the field gradient. During the first period, due to a mis-wiring in the Septum, the field gradient was different from expected. New compensation coils along the beam direction (z) and perpendicular to the beam in the horizontal direction (x) were added. With all the compensations, the

field gradients were reduced to a level that had little effect on the polarization and NMR, but still a significant depolarization effect when EPR was performed. We thus had to minimize the number of times EPR was performed during the first running period. The field gradient was much smaller during the second running period. Only at the highest Septum settings was a compensation field necessary to reduce depolarization effects during polarimetry measurements.

The average in-beam target polarization was slightly below 40% for the first period, and about 40% for the second running period. Other than the beam depolarization and the depolarization during polarization measurement due to the field gradient from the Septum, there were only few cases where significant depolarization occurred. During the first period, there was a problem in one laser line which caused two optical fibers to be burnt when the laser was in full power. The problem was traced to the wrong orientation of a quarter wave plate due to the wave plate being loose. It was fixed as soon as it was found. During the second period, there was one incident that the target polarization dropped significantly during a maintenance period; no apparent reason was found.

Collimators installed to block electrons scattered from the target cell end windows from getting into the spectrometer acceptance were very effective. The newly implemented optical fibers for the EPR system and for the spectra-analyzer also worked nicely during the experiment.

The target system was moved back to the target lab after the experiment. It has been set back up to get ready for tests for the next polarized ^{3}He experiment (E02-013, G_{En} [3]). Upgrades planned for the G_E^n experiment include:

- A new design of the main field magnet along with a shielding box to keep the BigBite spectrometer field away from the target region
- Associated mechanical system in the target region
- A new laser room outside the hall to replace the laser hut
- An optical fiber system for the lasers to go from the laser room outside the hall to the target region
- A new optical system to polarize the laser beam
- A new NMR system using RF sweep instead of the main field sweep
- Possible cell design changes: an increase in the pumping chamber to target chamber volume ratio and a shape change from spherical to cylindrical to increase laser pumping efficiency
- A possible change from Rubidium to K-Rb hybrid spin-exchange optical pumping.

Work on most of the above changes has started. The upgrades are expected to be ready by late next year for the planned G_{En} running in spring 2005.

3 General Hall Developments

3.1 Detector Developments

3.1.1 The E02-013 (G_E^n) Experimental Setup

Contributed by Kathy McCormick

Experiment E02-013, "Measurement of the Neutron Electric Form Factor G_E^n at High Q^2 [3]", is tentatively scheduled to take data in 2005. This experiment will extract the neutron electric form factor from a measurement of the cross section asymmetry in the $^3\vec{H}e(\vec{e},e'n)$ reaction. The experiment will detect the scattered electron in the Bigbite spectrometer and the recoiling neutron in a large area neutron detector which is being constructed at Jefferson Lab by the collaboration. The status of the main G_E^n subsystems will be described below.

- Neutron Detector
  A large area neutron detector is required to match the acceptance of the Bigbite Spectrometer. The design of the detector includes neutron bars from the University of Virginia (UVa), Jefferson Lab, Glasgow University (GU), and Carnegie Mellon University (CMU). The design at this time (Fig. 10) incorporates the bars into seven layers, with the thinner CMU bars forming the first four layers, followed by the UVA and JLab bars. The GU bars form a separate section of the detector, separate from the rest of the bars because of their different timing characteristics. Two layers of veto scintillators (not shown in the figure), will be mounted on the front of the detector for a charged particle veto. The active area of the full neutron detector will be 4.7 m (vertical) by 1.6 m (horizontal).

  A prototype of the neutron detector containing 20 UVa neutron bars (1.6 m long) was constructed by the collaboration and tested in Hall A in February, 2003. The main goal of the test was to study the neutron detector trigger rate as a function of the trigger threshold. The test was carried out under the exact conditions of our $Q^2 = 3.245$ (GeV/c)^2 data point, with a beam energy of $E = 3.028$ GeV and the neutron detector located at 25° (beam right), approximately 8 m from the target. The target was varied throughout the test run, first taking data on a BeO + ^{12}C multifoil target, then on a 40 cm polarized ^{3}He target cell. The total thickness of the polarized helium target is approximately 770 mg/cm^2. With a beam current of 0.5 μA and a trigger threshold of 50 MeVee, a trigger rate of 18 kHz was observed on the neutron detector. Extrapolating this to the running conditions of the experiment, 15 μA and a 10× bigger neutron detector, leads to a rate of approximately 5.4 MHz for the full detector. To keep the total DAQ rate below 3 kHz, the trigger rate on the neutron detector should not exceed ~ 1 MHz. To achieve this rate requires a drastic reduction of material along the

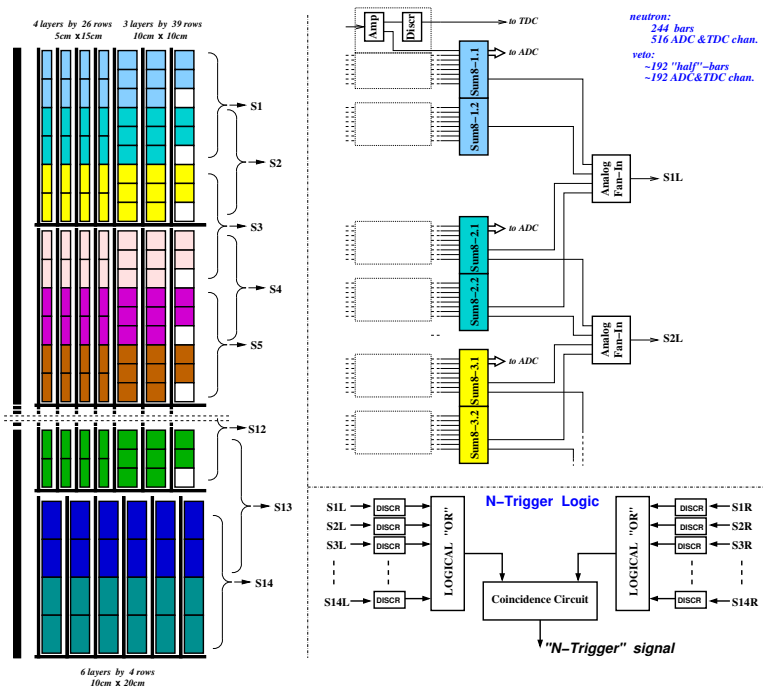

Figure 10: Preliminary layout of the G_E^n neutron detector. The electronics schematic is also shown.

beamline and in the detector acceptance. To minimize the material, the plan is to reduce the thickness of the beamline entrance and exit windows, put helium in the path of the beam instead of air inside the scattering chamber, and collimate the target glass windows out of the acceptance. It was also decided to move the detector back from 8 m to 12 m, increasing its size from 4 m to 4.7 m to partially compensate for the loss of acceptance. A preliminary design of the neutron detector has been proposed, and engineering began in early December, 2003.

- Polarized Target Development

  To shield the polarized helium target from the Bigbite fringe field, an iron box will be placed around the target region. With the addition of four sets of coils to the corners of the box, it will double as a holding magnet, producing the ∼30 G field needed to orient the target polarization vector. The magnetic properties of this system were modeled in both MAFIA and TOSCA and it appears from these models that the gradients are at a level tolerable for the polarized helium target system (i.e. 10 – 30 mG/cm). The iron box has been designed and ordered, and the coils have arrived on site at JLab. The box is expected to be set up in January, 2004, for testing and field-mapping.

  As mentioned in section 2.5, several major developments are planned for the G_E^n target system. These include changes to the cell geometry (from a spherical pumping chamber to a cylindrical one), changes to the optical pumping (from pumping Rb to pumping a mixture of K-Rb), and changes in the way NMR measurements are performed. The cell development is being studied at UVa and William and Mary. The change in the way the polarization is measured, from sweeping the holding field to sweeping the RF excitation field, is being studied throughout the polarized helium collaboration.

- Bigbite G_E^n Detector Stack

  The Bigbite detector stack for G_E^n will be the first to include chambers for high precision tracking. Three sets of MWDC are under construction at UVa. The first and third chambers will have 2 u, 2 v, and 2 x planes, with a resolution of ∼200 μm. The middle chamber will have u and v planes with $\sim$ 1 cm resolution to increase high-rate and multi-track capabilities. The first chamber is expected to be completed by the end of 2003. The design for the third chamber is underway.

  A lead glass shower and preshower detector are being added to the Bigbite detector stack to provide online PID reaching 98% for electron identification and pion rejection factors of 20-30. The preshower detector consists of 54

lead glass blocks, while the shower consists of 189 blocks. The array will be built in a close-packed configuration, with the preshower and shower subarrays sandwiching a plane of trigger scintillators. A representative of ITEP will arrive on site at JLab in early 2004 to begin the array construction.

3.1.2 Detectors for E00-110 (DVCS) and E03-106 (nDVCS)

Contributed by P. Bertin, C. Hyde-Wright, A. Camsonne, C. Muñoz Camacho, F. Sabatié and E. Voutier

During the past year, the E03-106 DVCS experiment on the neutron (nDVCS) was proposed and approved by the PAC and will most likely run following the proton experiment E00-110, currently scheduled to start in August 2004. In addition to the construction of the E00-110 detectors, a tagger system is being constructed specifically for E03-106. The next few paragraphs will detail the status of readiness of each subsystem for both experiments: the custom-built scattering chamber and detector support, the electromagnetic calorimeter, the scintillator array, the nDVCS tagger, the data acquisition system and finally the DVCS analysis software.

The E00-110 experiment needs a custom-built scattering chamber which will allow the detection of protons with momenta as low as 400 MeV/c. A 62 cm-diameter, 1 cm-thick spherical aluminum chamber has been designed for this purpose, and is planned to arrive at Jefferson Lab in April 2004. The DVCS detectors attach to a frame, which itself sits on a support structure, attached to the Big-Bite moving frame. Both the DVCS detector frame and the support structure will be at Jefferson Lab in December 2003, well before the installation of the detectors, which is planned for February 2004.

The electromagnetic calorimeter is composed of 132 blocks of PbF_2, stacked in 12 columns by 11 rows. This detector was assembled during the summer of 2003 and will be throughly tested until the end of 2003. First results from cosmic runs show that the photo-electron yield is above the Monte-Carlo expectations by about 20% with about 1200 p.e./GeV. The LED monitoring system showed promising performance after some necessary tune-up. Some repairs and improvements are necessary and it is planned to take the calorimeter apart, repair it and re-stack it in January 2004.

The proton/neutron detector consists of a 100-block scintillator array. The blocks are truncated trapezoids, arranged in 20 towers of 5 scintillators each. Each tower spans 13.5° in azimuth around the nominal virtual photon direction. Each scintillator in a tower spans 4° in polar angle. The scintillators are coupled to XP2972 PMTs. In order to cope with the large background of low-energy particles in the proton array, we are constructing an active base with the first two dynodes stabilized by a Zener diode/transistor circuit, and an electronic pre-amplifier of gain 30 (V. Popov, JLab). We will operate the HV in the range 650 to 800 V, (PMT gain 3×10^3 to 3×10^4). The total signal amplitude from DVCS protons ranges from 300 to 3000 photo-electrons. The towers, fully equipped with PMTs and electronics, are expected to be ready for installation in February 2004. The mechanical support for them is already available.

The nDVCS tagger is composed of 2 layers of 2 cm-thick EJ200 scintillator paddles. Each layer is segmented in 20 elements corresponding to the 20 towers of the scintillator array described above. The second layer is shifted by 1.5° compared to the first layer to avoid dead areas. An additional 1 cm-thick iron plate provides additional shielding to the tagger from direct view of the target. A prototype scintillator paddle was mounted and tested at LPSC Grenoble in order to improve the response of the detector in terms of light uniformity across the paddle. It was found that short light guides were necessary to improve the response, especially in the corners of the paddle. Also, aluminum foil was chosen as the best wrapping to shorten the pulse as much as possible, which is essential in the high rate environment. New prototypes with final dimensions and light guides will be tested before the end of 2003 and the design of the tagger system will be frozen before the end of the year. The scintillator paddles are planned to arrive at LPSC mid-March. By then, all components of the tagger should be there (mechanical assembly, light guides, phototubes, divider bases), and the assembly will proceed. The whole detector should be ready for tests sometime before mid-May; the planned shipping date to Jefferson Lab is May 31st. This leaves one month to re-mount the detector and the time between the end of June and the beginning of the E03-106 experiment in October 2004 for tests. Note that this schedule allows for the detector to be mounted in the Hall in its regular setup before both experiments start, which allows for an in-situ mechanical test.

The CODA data acquisition interface to the ARS, the trigger module(s) and the XY-table was completed in 2003, and was successfully tested with both LED and cosmics for the calorimeter in the fall of 2003. Some software is still needed, including the communication with EPICS for the high voltage, XY-table movement and LED setup. All this EPICS software is currently under development and should be ready by the end of 2003. The scintillator array and nDVCS tagger have not been plugged in the acquisition system, since they are not yet constructed. However, much of what has been done for the calorimeter can be mimicked for the other detectors, since most components are essentially the same. The next major step is the integration with the Hall A DAQ, which will be tested during the next down available in the first half of 2004.

The software scheme used for the E00-110 and E03-106 experiments resembles the RCS scheme: the spectrometer analysis will be performed in the first phase, either with ESPACE or with HANA. The analyzed data will be output in a ntuple-like structure, to be read in by the DVCS software package, which will perform the rest of the analysis. The calorimeter offline analysis software is ready and has been tested with Monte-Carlo data. Clustering algorithms along with energy and position calculations are available. The scintillator array geometry is fully implemented and the proton trajectory through the actual detector can be computed with the corresponding energy losses and light emission in each individual block. The ARS waveform analysis has been developed but needs to be integrated into the DVCS software package. Event displays are available for debugging and

on-line monitoring, but have only been tested with off-line data (Monte-Carlo, cosmics and LED runs). Most of the software efforts in the next few months will focus on the development of additional monitoring tools, which can be tested both with off-line and on-line data from cosmics and LED calibration runs.

Overall, the construction phase is on track and we expect to have the whole system - nDVCS tagger excluded - ready by the end of February 2004 for thorough tests and additional studies. The nDVCS tagger itself will be ready for tests in June 2004, well before the expected running date in October 2004.

3.2 Preparations for Hall A Parity-Violation Experiments

Contributed by K.D. Paschke

3.2.1 Polarized Source Development for Hall A PV Experiments

The Hall A parity program uses parity-violating (PV) processes as a probe into the structure of nucleons and nuclei. The experiments in this program place very stringent demands on the polarized electron source in order to achieve the necessary statistical precision and systematic accuracy. The more demanding of the currently-scheduled experiments, E99-115 (HAPPEX-II), will measure PV scattering from Hydrogen at $Q^2 = 0.1$ GeV$^2/c^2$, with a final statistical precision of about 50 parts per billion (ppb). Another PV experiment with conditional approval, PR-99-012 (Lead) is more demanding yet, with a goal of measuring the PV scattering asymmetry from Lead nuclei with a precision of 15 ppb in order to directly measure the extent of the neutron skin which is expected to exist in heavier nuclei.

In order to limit systematic errors to negligible levels for these measurements, it is necessary to both limit and correct for systematic helicity-correlated (HC) differences in the beam. The largest corrections are for the charge asymmetry, which is a HC difference in integrated current between two helicity windows of a pair, and the HC position differences. With the highly linear beam current monitors and phototubes of the integrating detectors, one expects to be able to correct for the charge asymmetry at the level of approximately 3%. Thus for HAPPEX-II, the charge asymmetry averaged over the entire data set must approach 0.6 parts per million (ppm), while for Lead the requirement is 0.15 ppm. The precision of the correction for position differences is limited by the precision in the coefficients relating position differences to measured asymmetry. Ideally, one would keep the size of the corrections at or below the size of the statistical uncertainty. The expected sensitivity to position on target is approximately 20 ppb/nm, leading to the requirement that, for HAPPEX-II, the HC position difference on target should average to about 2 nm over the entire run.

The effort to control HC systematics at this level focuses on both designing and tuning the polarized source to minimize HC effects, and implementing feedback loops on the source which can be used to minimize real-time measurements of HC systematics. Collaboration members have been working closely with the source group on these efforts. Beam tests have been performed with measurements in both Hall A and the injector to characterize performance of the source and the feedback mechanisms. The source group has also facilitated studies by collaboration members on the Injector Test Stand (ITS) Laser table to study possible improvements in the source optics.

A corrector mechanism for charge asymmetry, the Intensity Attenuator (IA) system, has been developed. It consists of two aligned linear polarizers with a $\lambda/10$

plate and Pockels cell between them. Relatively small voltage changes ($\pm$50 V) on the Pockels cell increase or decrease the intensity attenuation through this system at the level of a few tenths of a percent. The relatively low applied voltage reduces steering or ringing effects from the IA cell, so this system provides a clean method for reducing or increasing the input intensity for one helicity state relative to the other.

The IA system has been successfully used in an automated feedback loop to control charge asymmetry systematics. An example of the charge asymmetry during a run taken in June, 2002 and the running average of the charge asymmetry over that run is shown in Fig. 11. These tests indicate that the IA system is suitable for fine control of the charge asymmetry.

One drawback of the IA cell system is that the adjustment does not correct the fundamental cause of the charge asymmetry, which is predominantly a result of residual linear polarization in the laser incident on the strained GaAs photocathode. The voltage applied to the Circularly Polarizing (CP) Pockels cell can be adjusted to reduce the fraction of linearly polarized light, and thus control the charge asymmetry at the root of the problem. Such a correction should also reduce some causes of position differences and help prevent unmeasured, higher-order effects such as spot size or shape asymmetries from becoming significant. For the sake of tradition, feedback using the CP Pockels cell high voltage is usually called "PITA" feedback, in reference to the Polarization Induced Transport Asymmetry effect (a cause of charge asymmetry). To take advantage of the benefits of such an approach, the IA feedback will be used on a time scale of a few minutes to minimize charge asymmetry, and the PITA feedback will be used on a time scale of 8 hours to minimize the average IA cell setting, thus keeping source systematics small while controlling the charge asymmetry.

Development is also continuing for the control of the HC position differences. An attempt was made to develop a corrector mechanism for position differences, suitable for active feedback, based on a piezo-electric actuated mirror (PZT mirror). The effect of the mirror is dependent on specifics of the accelerator setup, and can be unstable over even short time periods. The system may be used for the passive control of position differences, with a retuning on time scales between 8 hours and 1 day, but it is not likely to succeed as an active feedback system with time scales on the order a few minutes.

Studies in the ITS laser room and with the CEBAF source and injector have been performed to investigate various sources of position differences and test approaches to minimizing these without feedback. Birefringence gradients in the CP Pockels cell have been shown to be the dominant effect in the particular set up used during the tests, producing position differences on the order of 1 μm in the 100 keV injector. Other sources such as birefringence gradients in the vacuum window, analyzing power gradients on the cathode, and steering effects were each estimated to contribute less than 200 nm during these tests, but may prove to be more significant in other configurations. Studies on the ITS laser table have been

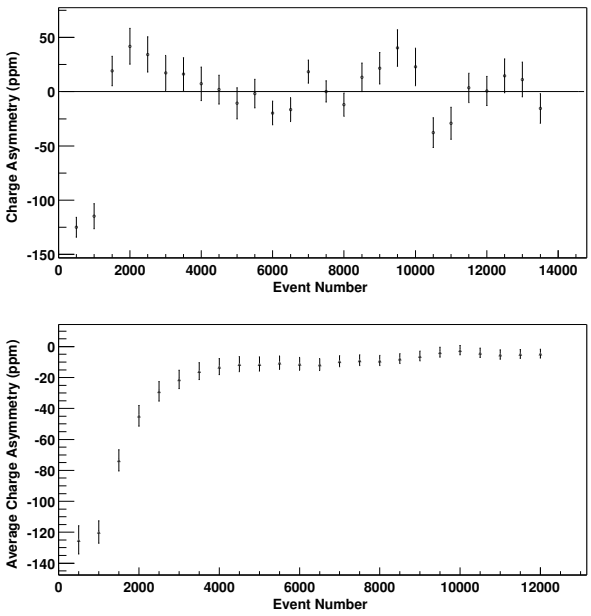

Figure 11: The control of the charge asymmetry and the convergence of the average charge asymmetry during a run from tests in June, 2002 demonstrate the effectiveness of feedback using the IA cell.

done to characterize new Pockels cells and select cells based on the qualities of importance, such as the birefringence gradients and steering properties, resulting in the purchase and selection of new cells with gradients a factor of 3 smaller than used in previous beam tests. Additional work on qualifying other optics elements and improving alignment procedures is expected to produce benefits. The design of the source laser optics may also be modified; imaging solutions which reduce the effective moment arm from the CP Pockels cell to the cathode would reduce the impact of steering effects, and configurations that reduce the beam spot size in the Pockels cell would reduce the effect of the birefringence gradients.

It appears very likely that the HAPPEX position difference goals are achievable. The new Pockels cells reduce the contribution from cell gradients by a factor of 3. Proper selection of source parameters can reduce these gradient effects by an additional factor of 2 and cathode gradients effects by estimated factors of 3-5. Steering effects from the new Pockels cells have been estimated from measurements on the laser table to contribute < 750 nm in the injector. This relatively large contribution may be reduced by an optics redesign which is currently being planned. In any case, steering effects will be efficiently canceled by slow-helicity reversal using an insertable half-wave plate. In addition, if the accelerator is well configured, the position differences should drop by a factor of approximately 95

during acceleration from the 100 keV injector to 3.2 GeV in the Hall due to the well-known adiabatic damping effect. Efforts to improve the machine setup in order to achieve that goal are on-going, but much progress has been made in reducing the mismatches and uncorrected skew effects which reduce the benefits from adiabatic damping. The Hall C G0 experiment, which will run in winter 2003-2004, will demonstrate the progress of this effort.

In addition to controlling the charge asymmetry and position difference averages, it is necessary to control other systematics that may increase noise or otherwise complicate analysis. One such effect is seen in Fig. 12, which shows the charge asymmetry as a function of time in the helicity window broken out by the time-ordering of the helicity states and the helicity of the window before the pair. The "asymmetric" pairs (for example, the pair RL following a R window) show a strong time dependence. Such an effect had previously been ascribed to to a slow settling of the high voltage on the CP Pockels cell. There is an additional effect in the significant difference between the "symmetric" pairs R(LR) and L(RL). In these pairs, each helicity window is preceded by its complement, so any effect of a slow high-voltage transition should affect these measurements in precisely the same way.

Further investigation of this effect has demonstrated that the slow settling of the Pockels cell birefringence is intrinsic to the Pockels cell and not related to a deficiency in the high voltage switch. The effect has been observed in Pockels cells made from KD*P and RTP crystals of various sizes and from multiple vendors. The "symmetric" pair difference is a manifestation of a history effect, where the charge asymmetry for a pair is systematically shifted depending on the ordering (RL or LR) of at least the two preceding pairs. This history effect has been observed to grow larger as the switching frequency is lowered and the cell sits at each setpoint longer. An example of this history effect on the charge asymmetry at 30 Hz is shown in Fig. 13.

Because it is highly symmetric, this multi-peaking in the charge asymmetry will not necessarily increase the systematic error due to the charge asymmetry correction. It has been shown that the separation between the peaks can be kept to a manageable level (< 1000 ppm) by proper configuration of source parameters, and a minor change of the helicity-flipping scheme has been made to more fully populate the region between the outer peaks in order to assist diagnosis of problems with this correction in analysis.

3.2.2 Data Acquisition and Analysis

The demanding statistical goals for HAPPEX-II require low electronics noise in the readout of the precision integrating ADCs. In order to limit pedestal noise, it was necessary to eliminate the long cable runs from the integrating electron detectors in the spectrometer hut to the parity DAQ in the counting house. Crates containing precision ADCs in each spectrometer have been added to the parity

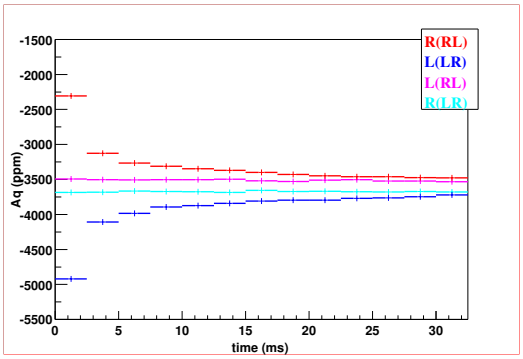

Figure 12: Time dependence of the charge asymmetry across the 33 ms helicity-flipping window.

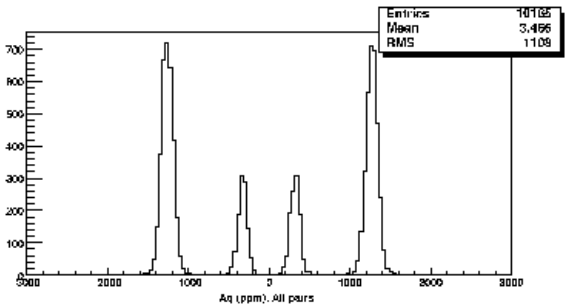

Figure 13: The charge asymmetry distribution displays multiple peaks caused by the history of pair ordering in previous pairs.

DAQ, allowing short cable runs and the opportunity to decrease noise pick-up. A crate in the injector has also been added to the DAQ, allowing the measurements of the beam positions and current in the injector to be made independently, or simultaneously with measurements in the Hall. This extension of the DAQ has proved to be an invaluable tool for the characterization of the source and of the accelerator setup.

To handle the additional monitors which have been added to the multi-crate DAQ, 2-MHz Voltage-to-Frequency (V2F) converters have been added for signals that do not require the higher resolution provided by the HAPPEX integrating ADCs. In order to extend the DAQ, it was also necessary to create new versions of the old HAPPEX ADC timing board. This board is used to gate the HAPPEX integrating ADCs and provide other DAQ control signals, based on an internal clock but triggered externally at the start of each helicity window. The new versions are largely functional copies of the old versions, with a few additional signal outputs useful for gating and latching scalers for the V2F readout. The new boards replace the old wire-wrap boards, which were becoming unreliable.

A new parity analysis package (PAN) has been developed, primarily written in C++ and making extensive use of the ROOT libraries. PAN was designed to serve as both a real-time on-line analysis tool, capable of providing online monitoring and controlling feedback systems, and an off-line analysis package. The online PAN functionality is nearing completion, while the off-line analysis functions are still under development. PAN incorporates a MySQL database of information for each run to track configuration changes and calibration parameters.

3.2.3 Detector and Beam Monitors

The integrating electron calorimeters have been built for the upcoming PV experiments. These detectors collect Čerenkov light from the elastic scattered electrons, and the absence of scintillation makes them insensitive to soft pions and photons. They are composed of alternating layers of fused quartz and brass so they are suitably radiation-hard, and they are specified to measure the energy of incident electrons with a resolution below 20%. A possible false asymmetry systematic due to trace ferromagnetic components of the brass alloy has been calculated to be negligible. The detectors are composed of two segments which will be aligned in the spectrometer focal plane to divide the Q^2 distribution. Each segment is instrumented with a single phototube. The combined detector will contain the distribution of elastically-scattered electrons while remaining separate from the inelastic distribution in the focal plane. The two segments connect to form an "L" shape, oriented so that the segments align with an edge of the Čerenkov cone for maximal light collection, as shown in Fig. 14. One segment was installed in the Møller polarimeter in Hall A for in-beam tests. These tests verified that the energy resolution was below 20%, and that edge effects were suitably understood.

A new set of luminosity monitors (lumis) have been installed on the beam line

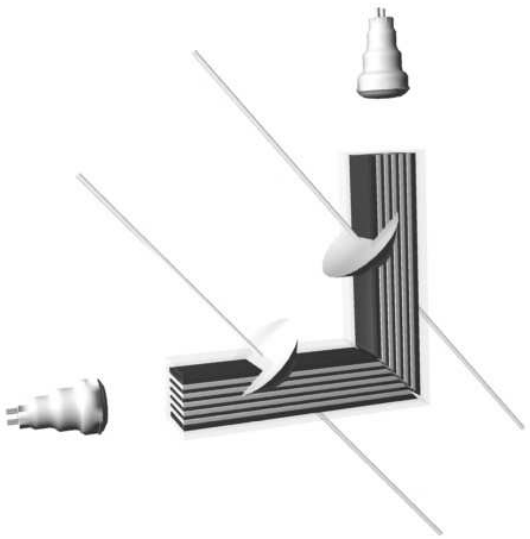

Figure 14: The two-segment HAPPEX detector.

downstream of the target. There are two sets planned: one at 0.5° and one at 6° scattering angles. The most forward-angle detectors will provide strong sensitivity to noise in beam parameters (more sensitive than the primary detectors), and the larger-angle set will monitor density fluctuations in the target and provide a test of electronics false asymmetry with an extremely narrow width signal. Both sets will be receiving rates in the range of 100 MHz at the HAPPEX luminosity. The monitors consist of individual small quartz Čerenkov detectors with air light guides to direct photons to a PMT. Eight such detectors will eventually be installed in the low-angle lumi, which sits approximately 7 m downstream of the target, while the large-angle lumi will consist of 2 detectors about 1 m from the target. Currently only two of the 8 detectors in the low-angle lumi have been installed.

In order to provide both higher resolution and higher redundancy in the measurement of charge and position, cavity beam monitors similar to those used in Hall B have been developed for both G0 and the Hall A PV experiments. The Hall A cavities have been installed, with two sets of cavities (each reading out charge and x and y positions) between the H04A and H04B stripline BPMs and a third set installed in the BSY region. New readout electronics for these cavities are currently being developed based on an I/Q mixer. These electronics should be available in January 2004, at which point these monitors can be commissioned. The monitors should be useful for all experiments in Hall A. They are expected to be of higher precision than the existing striplines, and because there is no multiplexing of signals in the readout electronics, they can be used to identify the beam location without using an algorithm to account for the raster phase as is currently necessary.

3.3 The Hall A RICH Detector

Contributed by Bodo Reitz

3.3.1 Introduction

JLab experiment E94-107, "High Resolution Hypernuclear Spectroscopy" [16] has been scheduled to run January until March 2004. Due to the high background from protons and pions in this experiment, the present HRS PID detector package consisting of two aerogel threshold Cherenkov detectors and scintillators for time-of-flight measurements is not adequate. Therefore, a proximity focusing RICH detector has been build. It uses liquid freon as radiator, a segmented CsI photocathode as photo converter and as cathode for a MWPC to detect the photoelectrons. This RICH detector is conceptually identical to one module of the ALICE-HMPID RICH [17]. A description can be found in the 2001 Hall A Report [18], the facilities for the handling of the CsI photocathodes are described in the 2002 Hall A Report [19].

3.3.2 Cosmic Test and System Improvements

The RICH detector was installed in the EEL building and regularly operated to perform test runs with cosmic radiation. Therefore system improvements could be tested immediately and long term changes in the detector performance could be monitored. The cosmic test were performed in the same manner as described in previous Annual Hall A Reports [18,19]. However, several improvements have been implemented.

- The front-end electronics have been rearranged in six groups instead of three, so that now groups of 240 (instead of 480) pads are read out sequentially by one ADC, reducing the associated deadtime by a factor of two. A second VME crate with the now necessary additional 12 CRAMS modules, a Sequencer and a Read-Out Controller has been set-up and tested. For the cosmic tests only one of the two VME-Crates (connected to one half of the electronics) was used at one time.

- A tiny leak between the radiator and the MWPC was detected, which decreased the performance of the detector. It was repaired and the freon vessel was reinforced. Additionally a second radiator was built, which will be used as a spare.

- The anode wire plane was re-strung with higher wire-tension, eliminating problems with individual loose wires not being able to hold high voltage. This problem was observed in earlier tests and resulted in the need to turn off those wires.

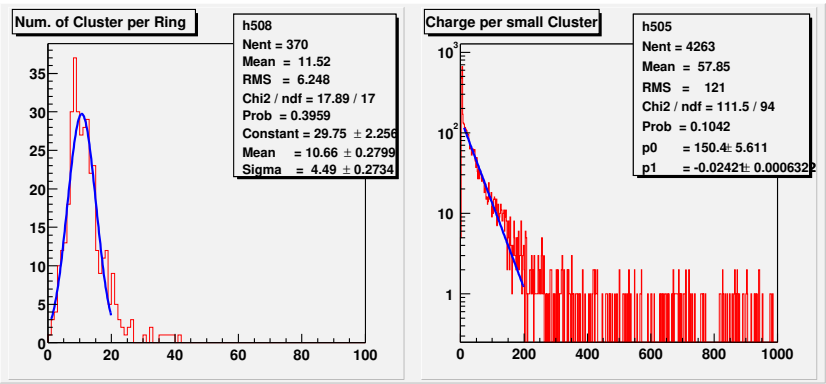

Figure 15: Distribution of the number of photo-electrons and of the charge per cluster for the cosmic tests in August 2003. The MWPC was operated at 2150 V with pure methane. The average number of photo-electrons per ring was 10.6.

Figure 15 shows results from a cosmic run performed in August 2003. The RICH was operated with pure methane as counting gas and a high voltage of 2150 V. At this high voltage the nominal gain ($\approx 8\ 10^4$ was achieved. The number of photo-electrons was 10.6 per ring, about 20% smaller than expected. It was also observed that the number of PE was slightly less in August as compared to the first measurements shortly after evaporation. This may have been caused by contamination of the counting gas with oxygen or moisture.

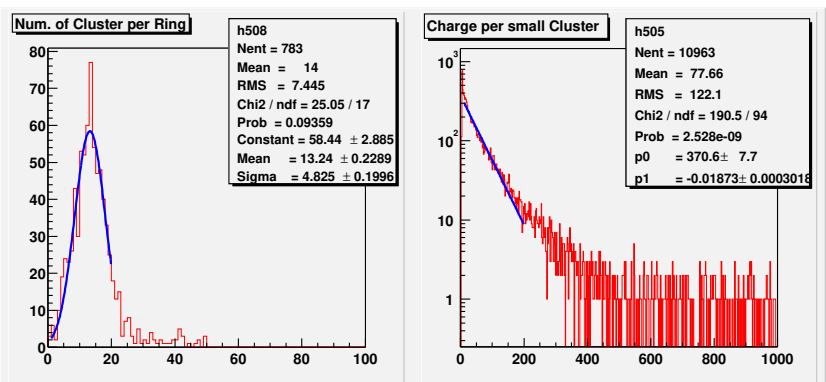

Figure 16: Distribution of the number of photo-electrons and of the charge per cluster for the cosmic tests in November 2003. The MWPC was operated at 2120 V with pure methane. The average number of photo-electrons per ring was 13.4.

In November three new photo-cathodes were evaporated and installed, together with a new anode wire plane, the latter being necessary to keep the gap between

cathode and anode at its nominal value. Due to mechanical intolerances the cathodes and wire planes have to be exchanged together. The new printed-circuit-boards used for this generation of photo-cathodes were manufactured with a new cleaning procedure, resulting in a 10% higher quantum efficiency after evaporation. Figure 16 shows the results from cosmic tests with these cathodes, the number of photo-electrons increases to 13.4 per ring, at the operating voltage of 2120 V. Under these conditions the charge per cluster is also larger than before. Figure 17 shows the event display of a single cosmic particle crossing the RICH detector, the cluster in the middle is the signal from the particle itself (Minimum Ionizing Particle or MIP), the clusters around it are caused by Cherenkov light. The previously used photocathodes have been re-evaporated, are safely stored in a dry and oxygen-free environment, and can be used as spares.

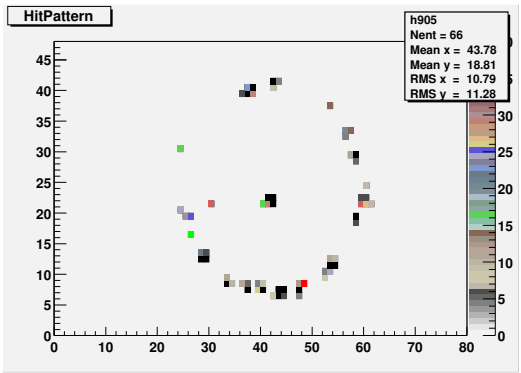

Figure 17: The event display for a single cosmic trigger. The large cluster in the middle is the signal from a MIP, the clusters around it are from the Cherenkov light.

3.3.3 Conclusions

The RICH detector for Hall A was successfully tested with cosmic radiation. The optimal operating parameters have been found, and it was shown that with cosmics the RICH performance meets its design specifications. For all critical parts of the detector (photocathodes, radiator) a full set of spares is available at JLab. The RICH detector is now (December 2003) installed in the left HRS of Hall A, and ready for the final in-beam commissioning and the use in experiment E94-107.

3.4 High Resolution Trigger Counter S2m

Contributed by R. Feuerbach

A need for an improved timing resolution was recognized after the initial set of experiments in Hall A. To address this need, the high-resolution S2m scintillator planes were designed to replace the original S2 trigger planes. In the Summer and Fall of 2003 these planes were fully assembled and installed in the HRS spectrometers; a picture of the completed S2m plane for the LHRS is shown in Fig. 18.

Figure 18: The fully assembled S2m scintillator plane in it frame, prior to installation into the LHRS. The on-frame discriminator can be seen mounted on the right.

3.4.1 Signal Processing

The signal path was designed to best preserve the timing of the pulses. The signals from each photo-multiplier tube are sent to a passive 90/10% splitter, with the greater portion sent to a P/S 706 discriminator on the detector frame and the lesser portion sent to the Fastbus ADCs. To form S2m's contribution to the trigger, the first discriminator output for each paddle's left- and right-side PMTs are logically AND'ed, and an OR over these results is performed. The right-side PMTs determined the timing of this trigger since their trigger-cables from the discriminator are 30 ns longer than those for the PMTs on the left side. The second output from the discriminator is sent through a NIM-ECL converter and an active ECL-delay module before being readout out by LeCroy 1875A TDC modules set to 50 ps/channel.

3.4.2 Results

During the second half of the GDH (E97-110) experiment, the LHRS was used as a luminosity monitor and data for the newly-installed S2m were taken parasitically. During this test, the TDC modules were set to 100 ps/channel. To measure the

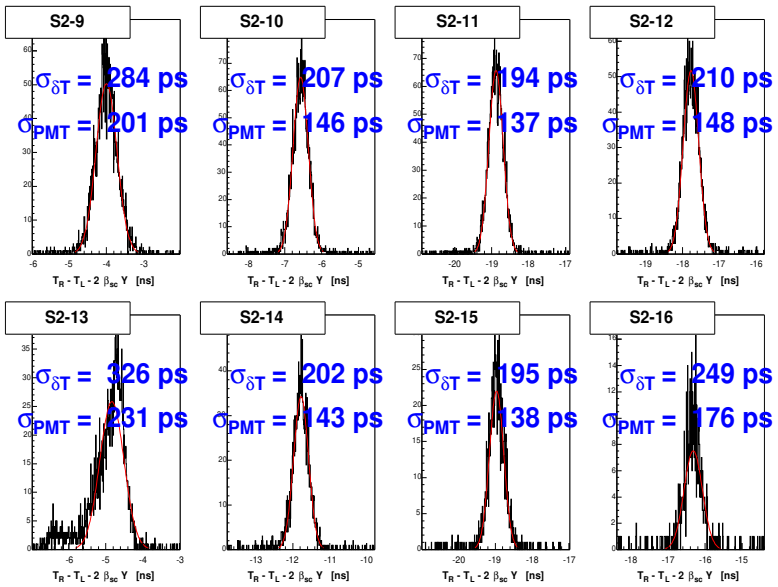

Figure 19: Distribution of the time-difference between the left- and right-PMTs on the upper eight paddles, after correcting for signal propagation through the scintillator.

inherent timing resolution, the time difference between the left and right-PMTs of each paddle was studied. After correcting for the signal propogation time through the scintillator, the width of the timing distribution was typically $\sigma_{L-R} \sim 210$ps. The distributions for the upper eight paddles, which are representative for all 16, are shown in Fig. 19. Under the assumption that both PMTs contribute equally to the width of the distribution, such that $\sigma_{L-R} = \sqrt{2}\sigma_{PMT}$, an average timing resolution-per-PMT of $\sigma_{PMT} \sim 170$ps was obtained. The expected timing-resolution of the the plane is then better than $\sigma_{s2} < 160$ps.

3.5 New Raster with No Dwell

Contributed by R. Michaels

Thanks to the efforts of Chen Yan (Hall C staff) and his collaborators, we successfully deployed a new fast raster in Hall A which is a copy of the Hall C design (Tech Note 97-004). This raster achieves a uniform rectangular density distribution of beam on the target by moving the beam with a time-varying dipole magnetic field whose waveform is triangular with very little dwell time at the peaks. This is a major improvement over our previous sinusoidal raster. The electronics design is an "H-bridge" in which switches are opened and closed at 25 kHz, to switch between two directions of current (100 A peak-to-peak) through the raster. The current is driven by HV supplies. At the moment one pair of switches is closed, the current rises according to the exponential law $(1 - e^{-Rt/L})$ where R = resistance, t = time, L = inductance. The current turns out to be highly linear for the choice of components. To switch the direction of current, one pair of switches are opened and another pair closed simultaneously and rapidly. The electronic and mechanical demands required state-of-the-art components: power terminal bus strips between HexaFETs, storage capacitors, polypropylene snubber capacitors, silver-plated thick copper terminals, and carefully designed pathways to reduce HV spikes and cross talk. The system has proven to be highly reliable in both Halls A and C.

3.6 Offline Analysis Software

Contributed by J.-O. Hansen

3.6.1 The C++ Analyzer

The first production release (1.0) of the new C++/ROOT-based object-oriented analysis software was completed in July 2003, followed by the first upgrade version (1.1) in November 2003. At this point, the C++ analyzer supports all the basic HRS and beamline instrumentation, including VDCs, scintillators, Cherenkov counters (both gas and aerogel), shower counters (both HRS arms), BPMs, and raster. Almost all of the functionality of our legacy FORTRAN software ESPACE is available. Thus, after over three years of development (with an average of one FTE), the C++ software is now essentially ready for production physics analysis. Experiment E94-107 (Hypernuclear Spectroscopy), scheduled to run in January 2004, will be the first experiment to use the new software. E94-107 particularly benefits from the new object-oriented design because of the new RICH detector, whose integration into the C++ analyzer is much easier than it would have been with ESPACE.

As the experimental configuration in Hall A is continually changing and entire new apparatuses (*e.g.* BigBite, G_E^n neutron walls, DVCS) are scheduled to be installed, the C++ analyzer was designed from the ground up to provide a high degree of modularity and flexibility, and in particular a clean and easy procedure for adding new detectors and apparatuses. To this end, we developed the concept of "analysis modules" that can be "plugged" into the analysis chain in almost any desired combination. An analysis module is either a detector, an apparatus (*i.e.* a collection of detectors such as a spectrometer or the beamline), or a "physics module" which performs post-reconstruction computations like kinematics calculations and energy loss corrections.

By organizing the analysis software as a collection of plug-in modules, the scope of the analysis is almost entirely configurable by the user instead of being pre-determined by the authors of the software. The configuration is typically set up at the beginning of an analysis script where the various desired modules are created and inserted into the appropriate analysis chain. No program code needs to be written or modified, and no recompilation is necessary, to change the configuration. Code for new equipment (*e.g.* the RICH detector) can be compiled into a separate shared library that can be linked dynamically at run time from within the analysis script. In this way, the analyzer can be extended as needed by each individual experiment without breaking the core system and without creating one of the notorious "private versions" of the software.

All standard detector classes have a generic design; for instance, the Cherenkov class can describe either a gas or aerogel detector with an arbitrary number of PMTs. For each actual Cherenkov detector, a new instance of the same Cherenkov

class is created, differing only in its name and database entries. Only one implementation of detector code exists and can be found in one obvious location (the detector class), so that updates can be applied and bugs can be fixed in one central place. The code and data scattering and "cut-and-paste" programming typical of ESPACE is avoided. From the user's perspective, it is no longer necessary to write *any* program code to add a new standard detector to an apparatus (*e.g.* a third scintillator plane to either HRS); only the appropriate database entries need to be created and a line be added to the analysis script. Furthermore, if certain equipment (*e.g.* left-arm HRS, shower counters in right-arm HRS) is not used by an experiment, there is no need ever to instantiate the corresponding modules, and so no overhead whatsoever is incurred in terms of memory usage and computation speed for unused features. The same holds for physics computations (say, extended target corrections) that a given experiment does not need. Conversely, it is possible to perform the same kind of physics computation several times with different parameters in the same analysis pass, *e.g.* the calculation of electron kinematics with and without energy loss corrections.

Performance tests show that the speed of the C++ analyzer is comparable to that of ESPACE. In some cases, a significant speed advantage of a factor of two or more was observed, in part due to the superior control over the analysis flow in the C++ analyzer where uninteresting events can be detected and skipped early in the processing chain.

The minor discrepancies between the tracking results of ESPACE and of an early version of the C++ analyzer, which were reported in last year's status report, have been understood and resolved. They were found to be due to calibration differences and small bugs in the C++ tracking code. Tracking results obtained with the current C++ analyzer and with ESPACE are shown in Figs. 20 and 21. The same optics database was used for both replays, and only "clean" events with one cluster per VDC plane were selected. The data analyzed were taken in September 2000 as part of an optics study with a 9-foil carbon optics target and the standard sieve slit collimator on the left-arm HRS. The beam energy was 825 MeV, the scattering angle, 16°, and the spectrometer central momentum, 838 MeV (elastic kinematics with a δ-offset). For ease of comparison, this is the exact same data set as in last year's report.

Figure 20 shows an overlay of the reconstructed target variables from the C++ analyzer and from ESPACE. As one can see, the agreement between the two sets of results is excellent. Figure 21 depicts event-by-event differences of the same quantities. The width of each distribution is about one order of magnitude smaller than the measured spectrometer resolution for the corresponding variable. Hence, the different tracking algorithms of C++ and ESPACE have negligible effect on the precision of the target reconstruction.

During the summer of 2003, an event display was developed as part of a student project. Such a visualization tool is useful for detector and tracking diagnostics and for online data monitoring. An example plot is shown in Fig. 22. The event

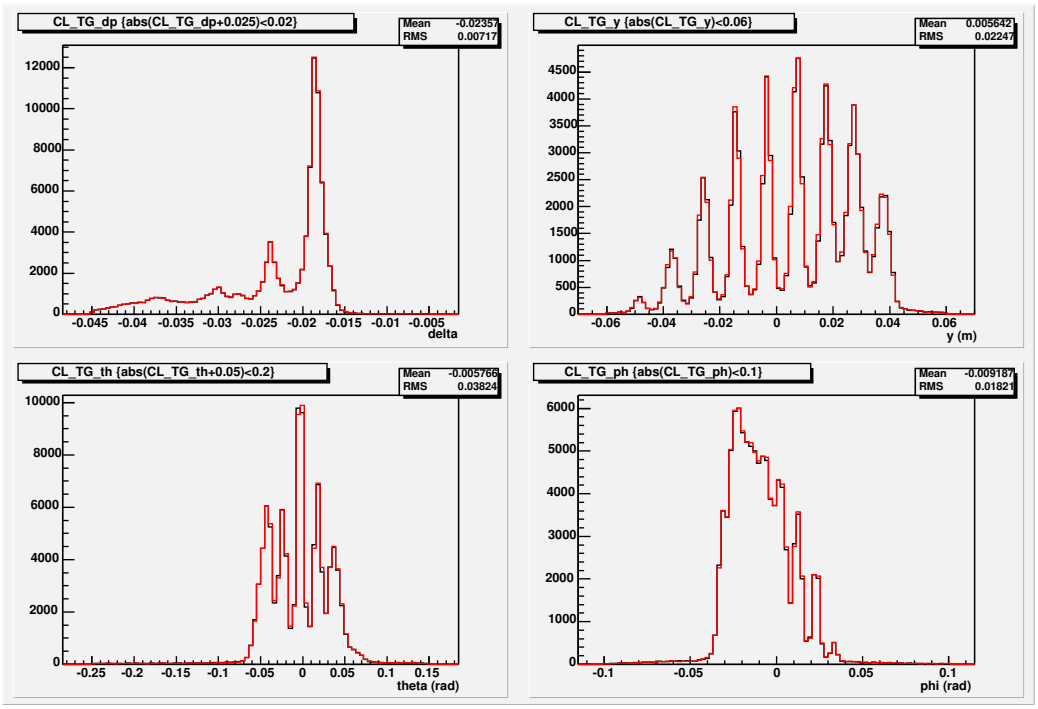

Figure 20: Results for the reconstructed target quantities δ (momentum), y (in-plane position), θ (out-of-plane angle), and ϕ (in-plane angle). The data are from an optics study that used a 9-foil carbon target and the sieve slit collimator on the left HRS (see text). In each panel, black histograms represent results from the C++ analyzer, and red (lighter colored) histograms were obtained with ESPACE. Since the results are nearly identical, the two histograms are almost indistinguishable.

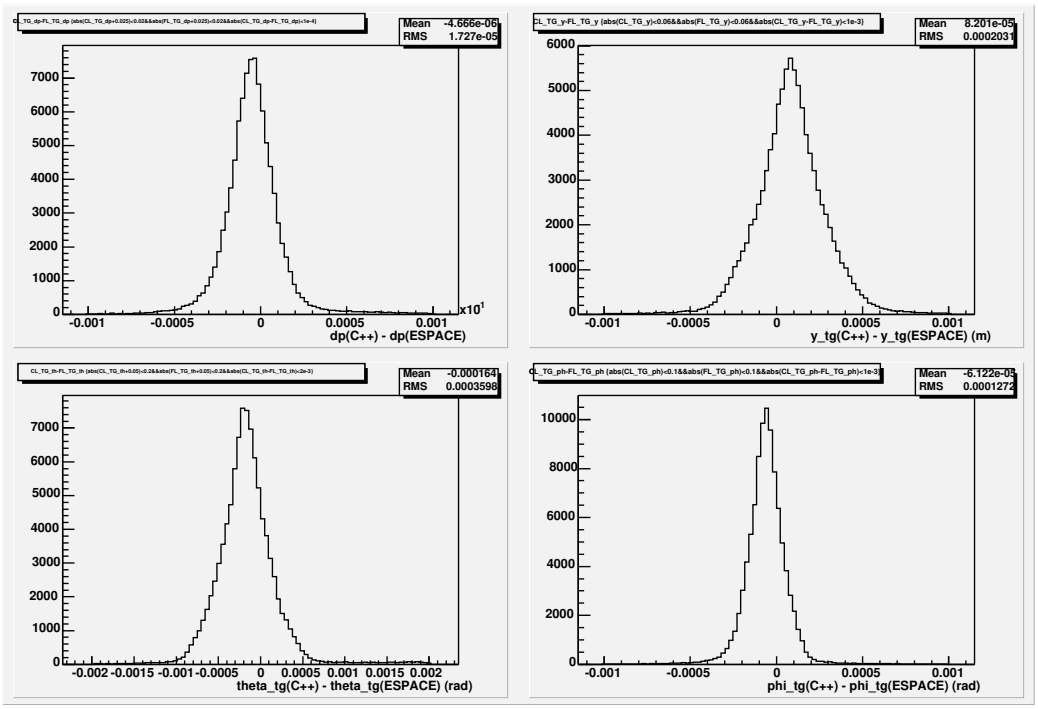

Figure 21: Histograms of the event-by-event differences of the target variables reconstructed by the C++ analyzer and by ESPACE. The data are the same as in Fig. 20. The widths of the distributions are about an order of magnitude smaller than the measured spectrometer resolutions for each variable.

display software is still in the prototype stage, but, once stable, we intend to include it in the official C++ analyzer.

Compared to ESPACE, the C++ analyzer still lacks several features: full multi-cluster/multi-track VDC analysis; full shower cluster analysis with multiple possible clusters; energy loss corrections; FPP analysis; and calibration and optimization utilities. All these items are important and will hopefully be implemented over the next year. Writing the FPP code is arguably the most difficult of these tasks. Fortunately, no experiment requiring the FPP is scheduled in the near term.

In addition to the gains in modularity and flexibility, the functionality of the new analyzer is expected to exceed that of ESPACE eventually. The dynamic output module available in version 1.1 is already more powerful than the corresponding COOLHANDS package in ESPACE. For the VDC analysis, we plan to add capabilities to suppress noise hits and to split overlapping clusters, which should improve the tracking efficiency at high trigger rates. The coincidence time analysis will take advantage of the relative timing between the trigger and the beam bucket clock for precision pathlength corrections. Finally, a likelihood analysis of particle ID could be added to appropriate detector classes. Suggestions for other improvements are welcome.

In the next several months, efforts will focus on the VDC tracking code and on testing and documentation. Up-to-date information about this project can be found on the Web [20]. Our manpower is limited, and volunteers are always welcome to join, especially those with some background in C++ programming.

The work reported here was carried out in collaboration with R. Michaels and R. Feuerbach from Hall A and SULI summer student R. Stringer from CSLA.

3.6.2 ESPACE

Our legacy FORTRAN-based analysis software ESPACE was updated for the Spin Duality and small-angle GDH experiments by Seonho Choi from Temple University, who added a sophisticated analysis of the beam helicity data (G0 helicity scheme). Currently, the new code is only available privately, but it will become official after review and testing of the changes. (Our policy is that a given official ESPACE version should be capable of analyzing all data taken in Hall A before approximately its release date. Therefore, new contributions must be tested for backward compatibility.)

Several items remain on the to-do list for ESPACE. In particular, a port to the high-performance auto-parallelizing Intel Fortran compiler is planned. We are committed to maintaining ESPACE for the foreseeable future as a re-analysis tool for older experiments. New experimental equipment will not be officially supported in ESPACE after 2003.

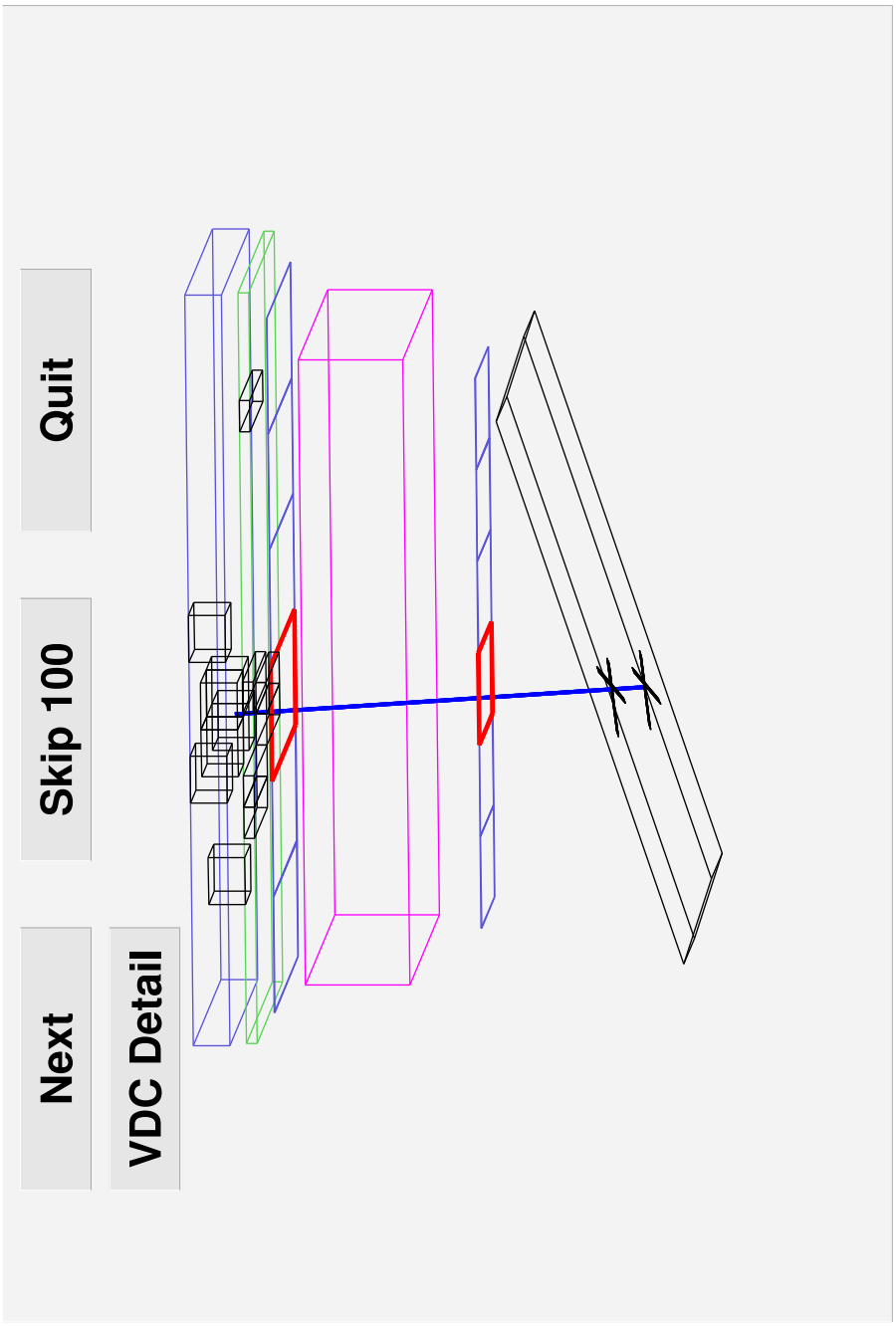

Figure 22: Example of a good track in the HRS visualized by the prototype event display of the C++ analyzer. Wire chamber clusters as well as active scintillator paddles and shower blocks are shown. The track is drawn using the reconstructed focal plane coordinates from the VDC.

3.7 DAQ in Single Arm Mode

Contributed by R. Michaels

During 2003 we ran two single-arm experiments (Spin Duality and GDH) for which the spectrometer DAQs ran independently. We were able to achieve a significant increase in the DAQ speed by making the following improvements and compromises. This is potentially relevant for parity experiments in counting mode (as opposed to integrating mode).

- We split up the modules in the fastbus crates so that they are evenly divided among crates. The deadtime (DT) of the system is the maximum deadtime of its crates.
- We dropped the high resolution TDC model 1875 which was not needed for those single-arm experiments. It is the slowest module in the crate with frontend DT of 50 ns, as opposed to 10 ns for the other modules, and and the scintillator signals were put into the 0.5 ns TDCs instead. This cannot be done for coincidence experiments.
- The beamline DAQ was all contained in fastbus, no more VME. The absence of the VME crate reduced the deadtime at intermediate rates (1-2 kHz) though it had no impact on the maximum speed.
- We ran in buffered mode. There were multiple redundant checks on the synchronization.

Observed Rate (kHz)	Prescale	Measured DT (%)	Model DT (%)
2.3	1	6.2	6 – 8
2.6	1	7.0	7 – 9
3.2	4	1.3	0.3 – 1.0
3.5	1	9	9 – 13
4.6	2	4.0	2.5 – 5.0
5.5	4	2.0	0.8 – 2.6
6.3	4	2.0	1.2 – 3.0
6.4	2	8.0	5 – 9
5.7	1	15	15 – 21
9.4	5	27	7 - 32
11	5	21 – 27	21 – 43
15.7	4	25	35 – 57
18.0	4	36	39 – 62

Table 1: DAQ Deadtime in Single Arm Mode

Generally the experience with buffered mode was good, particularly for the right spectrometer. On the left spectrometer there is an unsolved problem of noise in one of the fastbus crates, leading to occasional extra hits in the modules. In addition, during one weekend the left arm DAQ lost synchronization, those data are recoverable with difficulty; the reason was never found.

A model based on Poisson probability could predict the deadtime, including for the case of prescale factor greater than 1. If the observed rate was below the maximum speed of the readout ($\sim$4 kHz in this mode) the deadtime (DT) is well behaved and kept below 10%. Above the maximum speed of the readout, however, the DT increased rapidly. Comparisons of the model with the measurements is shown in Table 1. The agreement is good in most cases.

4 Summaries of Experimental Activities

4.1 E89-044

Selected Studies of the $^3He(e,e'p)$ Reaction

M. Epstein, A. Saha, and E. Voutier, Spokespersons

The E89-044 experiment took data from December 1999 up to April 2000 investigating the origin and the importance of the high momentum components in the ^{3}He nucleus, both in the 2-body and 3-body break-up channels. Different kinematics were studied: in quasi-perpendicular kinematics we measured a missing momentum distribution up to about 1 GeV/c in recoil momentum together with the separation of the R_T, R_{LT}, and R_{L+TT} response functions, and the measurement of the A_{LT} asymmetry. In parallel kinematics a Q^2 dependence was measured at 0 and $\pm$300 MeV/c recoil momentum and the R_L and R_T response function were separated.

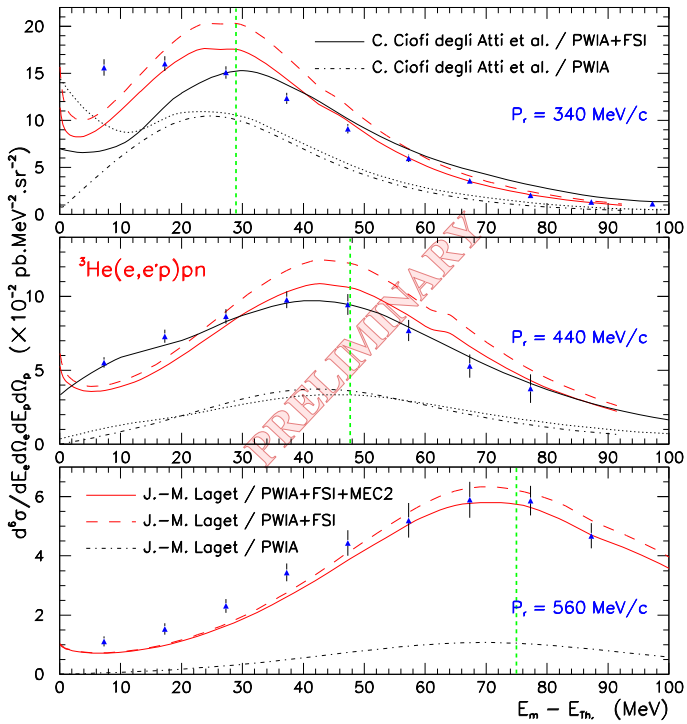

Figure 23: Sample of the 3-body break-up data [22] for several recoil momenta. Theoretical calculations are shown for different approximations of the (e,e'p) reaction process. The green dashed line indicates the expected position of the maximum of the cross section assuming a correlated pair in the nucleus.

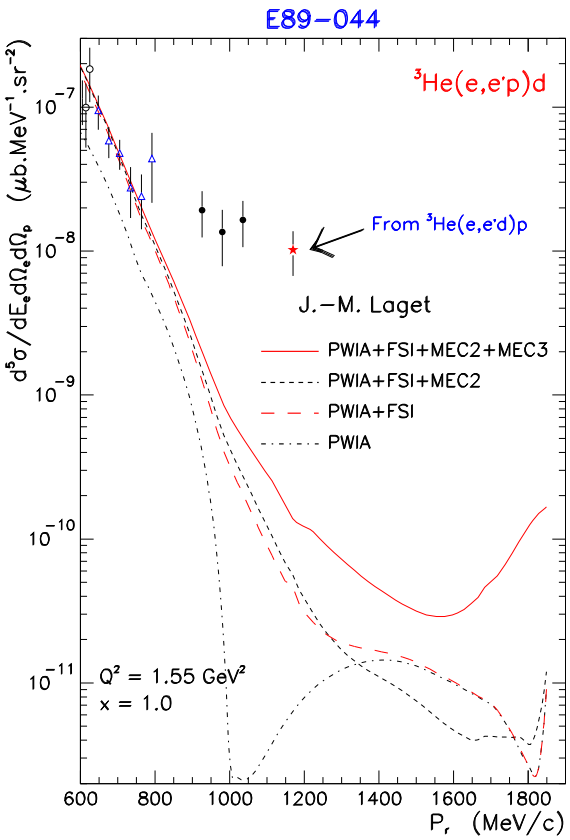

Figure 24: Very high recoil momentum distribution in ^{3}He; triangle and dot symbols are ^{3}He(e,e′p)d analysis results [21] and the star symbol of the last point is the reconstructed cross section from the ^{3}He(e,e′d)p measurement.

Major progress has been accomplished during this year with the completion of the analysis of perpendicular data in the 2-body break-up channel [21],and the almost complete analysis of parallel cross section.
The main new features come from the release of the 3-body break-up channel analysis [22], partly shown on Fig. 23. The location of the maximum of the cross section is consistent with older experimental data [23] suggested that the dominant contribution to the cross section in this reaction channel comes from the interaction of the virtual photon with a correlated pair in the nucleus. However, the main new feature is, contrary to original thought, that as the recoil momentum increases the bulk part of the cross section comes from the rescattering of the knocked-out proton. This is in clear agreement with the 2-body break-up data [21] and the new deuterium data [24] which generally confirms that our quasi-perpendicular data are dominated by final-state interactions in the mid-range of our measured

missing momenta distributions.

An unexpected result was also obtained from the analysis of the ^{3}He(e,e′d)p channel for which we have data for the spectrometer settings used to measure the highest recoil momenta kinematics for the ^{3}He(e,e′p) data. For this specific setting the knocked-out proton and the recoil deuteron have very similar momenta and are detected simultaneoustly by the hadron HRS. One can then measure the (e,e′d) cross section and deduce the corresponding $^3He(e,e'p)d$ cross section. The resulting data point [25] is plotted on Fig. 24 together with Σ_1 results. Since the proton coresponding to the deuteron is on the left side of the virtual photon, this data point is not strictly comparable to the Σ_1 data measured on the right side of q. It only confirms the magnitude of the cross section at very high recoil momentum and the very large deviation from theoretical expectations.

4.2 E91-011

Investigation of the $N \rightarrow \Delta$ Transition via Polarization Observables in Hall A

S. Frullani, J.J. Kelly, and A.J. Sarty, Spokespersons

We have measured recoil polarization in the $p(\vec{e}, e'\vec{p})\pi^0$ reaction at $Q^2 \sim 1$ $(\mathrm{GeV}/c)^2$ near the Δ resonance, obtaining angular distributions for a total of 16 independent response functions in a 5×2 grid of (W, Q^2). Although not statistically independent, we have also obtained response functions for a single bin, defined by $W = 1.23 \pm 0.02$ GeV and $Q^2 = 1.0 \pm 0.2$ $(\mathrm{GeV}/c)^2$, that is centered on the $\Delta(1232)$ resonance. The data analysis has been discussed in previous progress reports and is almost finished, with just a few consistency checks remaining. Drafts of a PRL and a PRC paper are in preparation.

Preliminary angular distributions for $(W, Q^2) = (1.22 \pm 0.2, 0.9 \pm 0.1)$ are shown in Fig. 25 versus $x = \cos\theta_{cm}$. The 12 response functions shown in columns 2–4 have been observed here for the first time. The response functions in the third column depend upon real parts of interference products and are dominated by resonant amplitudes while those in the second and fourth columns depend upon imaginary parts and are more sensitive to the nonresonant contributions.

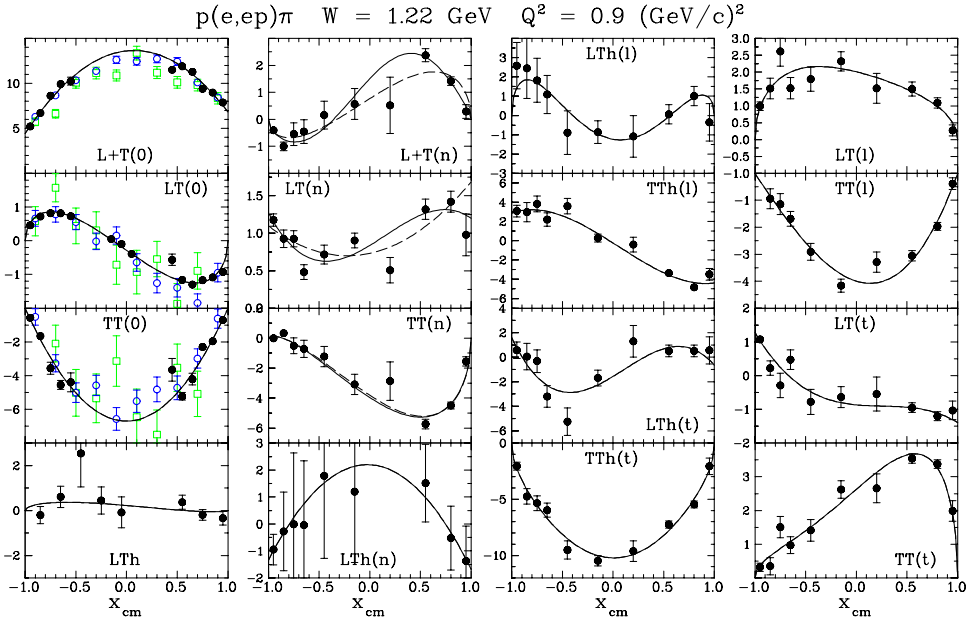

Figure 25: Data for response functions at $W = 1.22 \pm 0.02$ GeV and $Q^2 = 0.9 \pm 0.1$ $(\mathrm{GeV}/c)^2$ are compared with Legendre fits in the *sp* truncation (dashed) and with a few extra terms as needed (solid). Results from CLAS are shown as green squares for $k_i = 1.645$ GeV or blue open circles for $k_i = 2.445$ GeV.

The unpolarized response functions are compared with the published Hall B data of Joo *et al.* [26]. Note that the Hall B data for R_{L+T} contain two beam energies while the Hall A data for $\epsilon \sim 0.95$ lie slightly higher, as expected. In general we find good agreement between the two experiments, but the statistical precision of the present data is considerably higher than that of the published Hall B data; higher statistics from the latter will be forthcoming. The limited spectrometer acceptance in ϕ for $x \sim 0$ does not permit separation there between R_{L+T} and R_{TT}, but the cross section data (not shown) were included in the partial-wave and multipole analyses.

Two types of analyses have been performed. In Fig. 25 we compare the data with fits based upon Legendre expansion of the angular dependence of each response function independently, while in Fig. 26 multipole amplitudes for low partial waves were fit to all of the data for a given (W, Q^2) bin simultaneously with higher partial waves based upon MAID2000 [27]. Both analyses describe the data well, but the Legendre fits are sometimes better because this more phenomenological representation ignores the correlations between Legendre coefficients for different response functions expected from expansions of those coefficients in terms of products of multipole amplitudes. The multipole analysis is more fundamental and employs fewer parameters.

Most previous analyses in the Δ region have limited the expansions to s- and p-waves and have used the assumption of M_{1+} dominance to truncate these expansions to terms involving the M_{1+} amplitude. Thus, using the coefficients fitted to the unpolarized cross sections one would deduce

$$EMR = \frac{\Re E_{1+}^* M_{1+}}{|M_{1+}|^2} \approx \frac{3A_2^{L+T} - 2A_0^{TT}}{12A_0^{L+T}} \quad (1)$$

$$SMR = \frac{\Re S_{1+}^* M_{1+}}{|M_{1+}|^2} \approx \frac{A_1^{LT}}{3A_0^{L+T}} \quad (2)$$

where A_n^α is the coefficient of P_n in the expansion of response function α. Our nearly complete set of recoil-polarization response functions makes it possible to perform a more rigorous multipole analysis. The sensitivity of fitted multipole amplitudes to uncertainties in higher partial waves can be gauged by comparing fits using different baseline models for higher partial waves. An advantage of this type of analysis is that it minimizes the dependence upon models; however, it does not guarantee that the fitted multipole amplitudes will depend smoothly on both W and Q^2. Model-dependent analyses which adjust parameters of an effective Lagrangian should produce kinematically smooth multipole amplitudes at the expense of possible bias.

The dashed lines in Fig. 26 show a fit that varies all s- and p-wave multipole amplitudes for $(W, Q^2) = (1.22, 0.9)$ while the solid lines vary d-wave amplitudes also. MAID2000 was used as the baseline model for higher partial waves. There appears to be no systematic improvement in the fits by varying d-wave ampli-

tudes but the fits are not as accurate as the Legendre analysis either, which may indicate a deficiency of the nonresonant contributions to the baseline model or inconsistencies in the preliminary data.

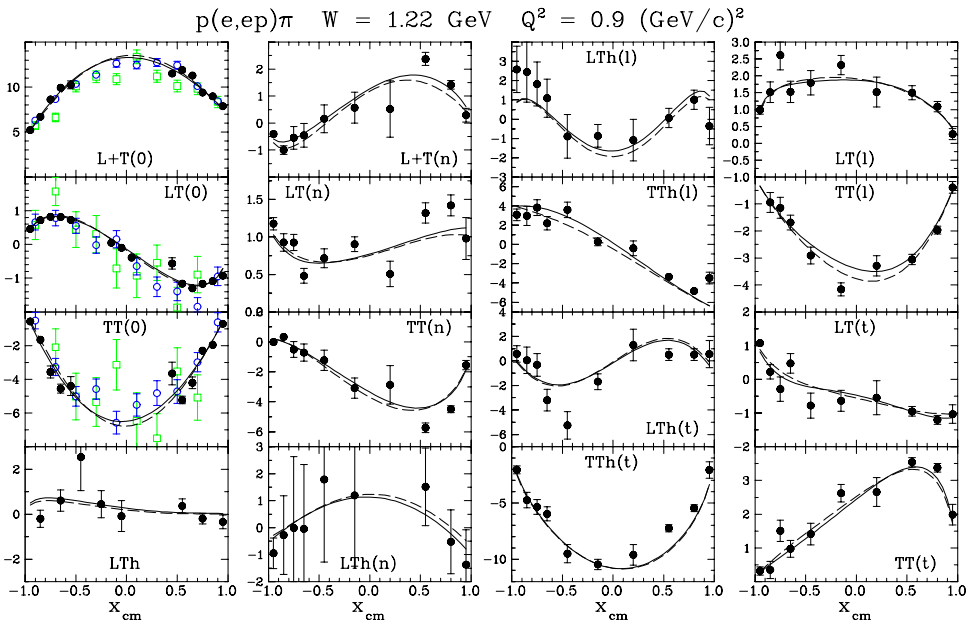

Figure 26: Data for response functions at $W = 1.22 \pm 0.02$ GeV and $Q^2 = 0.9 \pm 0.1$ $(\mathrm{GeV}/c)^2$ are compared with fits that vary *sp* (dashed) versus *spd* (solid) multipole amplitudes. Results from CLAS are shown as green squares for $k_i = 1.645$ GeV or blue open circles for $k_i = 2.445$ GeV.

The quadrupole deformation parameters can now be obtained directly from the fitted multipole amplitudes using

$$EMR = \frac{\Re E^*_{1+} M_{1+}}{|M_{1+}|^2} = \frac{\Re E_{1+}\Re M_{1+} + \Im E_{1+}\Im M_{1+}}{\Re M_{1+}\Re M_{1+} + \Im M_{1+}\Im M_{1+}} \quad (3)$$

$$SMR = \frac{\Re S^*_{1+} M_{1+}}{|M_{1+}|^2} = \frac{\Re S_{1+}\Re M_{1+} + \Im S_{1+}\Im M_{1+}}{\Re M_{1+}\Re M_{1+} + \Im M_{1+}\Im M_{1+}} \quad (4)$$

where $\Re M_{1+} \to 0$ at the physical mass, $W \to M_\Delta = 1.232$ GeV. The deformation of the $N \to \Delta$ transition is generally quoted at $W = 1.232$ GeV after correction for the isospin-1/2 contribution, but this correction has not yet been made.

These two methods for determination of EMR and SMR are compared in Fig. 27. The left panel uses the truncated Legendre analysis while the right panel uses the multipole analysis. We also extracted EMR and SMR for the MAID2000 [27], DMT [28], and SAID [29] models by applying the same formulas to calculations that were used for data in each panel. The difference between the two methods at $W = 1.232$ GeV is a measure of the accuracy of the truncated Legendre analysis.

The experimental results for SMR are stable and both methods give similar W dependencies over this entire range. The model calculations for SMR are also in agreement with the data near 1.232 GeV and describe the W dependencies well, although MAID2000 and DMT are in better agreement with each other than with SAID. For EMR, on the other hand, the two methods produce different W dependencies and the variation among models is greater; nevertheless, these variations remain fairly small in the immediate vicinity of M_Δ. The experimental results are more sensitive to the choice of variables and baseline model for EMR than for SMR. The red stars were obtained from the bin centered on the Δ and are consistent with interpolation among the black points. Although at this Q^2 truncated Legendre analyses appear to be sufficiently accurate for extraction of EMR and SMR, the present data for helicity-independent recoil polarization do show significant deviations from models and sensitivity to the relative phase between resonant and nonresonant amplitudes.

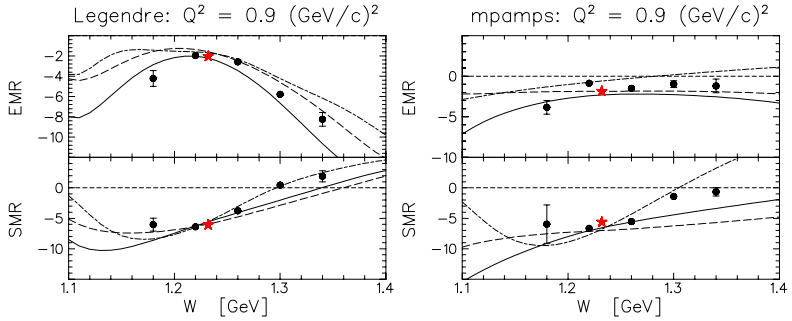

Figure 27: EMR and SMR data for $Q^2 = 0.3$ (GeV/c)^2 are compared with MAID2000 (solid), DMT (dashed), and SAID (dash-dot). In addition, the red star shows the result for $W = 1.23 \pm 0.02$ GeV, $Q^2 = 1.0 \pm 0.2$ (GeV/c)^2. Left: results from truncated Legendre expansion. Right: results from multipole analysis varying sp amplitudes w.r.t. MAID2000. Within each panel data and curves employ the same formulas.

4.3 E93-050

Virtual Compton Scattering from the Proton

P. Bertin, P. Guichon and C.E. Hyde-Wright, Spokespersons

In E93-050, we measured the angular distribution of the H$(e,e'p)\gamma$ reaction below pion threshold at $Q^2 = 1$ and 2 GeV^2 at an incident energy of 4 GeV. In addition, with the recoil proton parallel to the momentum transfer q from the electron, we measured an excitation curve in the nucleon resonance region at $Q^2 = 1$ GeV^2, and the Q^2 dependence of the cross section in the vicinity of the S_{11} resonance.

According to the low energy theorem of Guichon, Liu, and Thomas, an expansion of $e + p \rightarrow e + p + \gamma$ in powers of the final photon energy depends lo lowest order only on the on-shell nucleon elastic form factors, and a set of generalized (Q^2-dependent) polarizabilities [30]. The dispersion relation formalism of Pasquini *et al.*, gives a complete description of the $e + p \rightarrow e + p + \gamma$ amplitude up to two-pion threshold in terms of just the nucleon born terms, the generalized electric and magnetic polarizabilities, and the $\gamma N \rightarrow N\pi$ multipole amplitudes (for both real and virtual photons) [31].

The E93050 collaboration has submitted two draft letters on the Generalized Polarizabilities to the Hall A collaboration for review:

- "Measurement of the Generalized Polarizabilities of the Proton in Virtual Compton Scattering at $Q^2 = 0.92$ and 1.76 Gev^2:
  I. Low Energy Expansion Analysis", S. Jaminion, *et al.*.
  "II. Dispersion Relations", G. Laveissiere, *et al.*.

The E93050 collaboration has a draft paper for review on the H$(e,e'p)\pi^0$ reaction:
"Backward Electroproduction of π^0 Mesons on Protons in the Region of Nucleon Resonances at Four-Momentum Transfer Squared $Q^2 = 1.0$ GeV^2", G. Laveissiere, *et al.*, nucl-ex/0308009.

We also have a draft letter on the excitation curve of the H$(e,e'p)\gamma$ reaction in the nucleon resonance region. Figure 28 displays the ratio of the H$(e,e'p)\gamma$/H$(e,e'p)\pi^0$ cross sections in the backward direction at $Q^2 = 1.0$ GeV^2. The P_{11}-Roper and $S_11(1535)$ (or D_{13}) resonances are very prominent in this ratio. The rise in Fig. 28 below the $P_{33}(1232)$ Δ-resonance is a consequence of the large Bethe-Heitler contribution. However, above the Δ, the Bethe-Heitler is negligible. Thus it is very significant that the cross section ratio is an order of magnitude greater than the $\Gamma(N^* \rightarrow N\gamma)/\Gamma(N^* \rightarrow N\pi)$ ratio of branching fractions. The differential cross section for each process is a coherent superposition of all open channels, whereas the branching ratios are incoherent.

One of the motivations for the study of the VCS excitation function was to explore the high W region, where the current quarks (rather than constituent

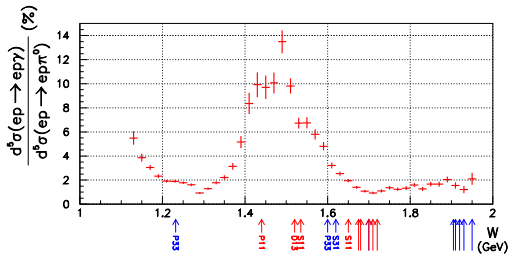

Figure 28: Cross section ratio $H(e,e'p)\gamma/H(e,e'p)\pi^0$, at $Q^2 = 1.0$ GeV^2 in a bin $\cos\theta_{\gamma p}^{CM} > 0.95$, where $\theta_{\gamma p}^{CM}$ is the angle between the recoil proton and the virtual photon q in the photon-proton Center-of-Mass frame.

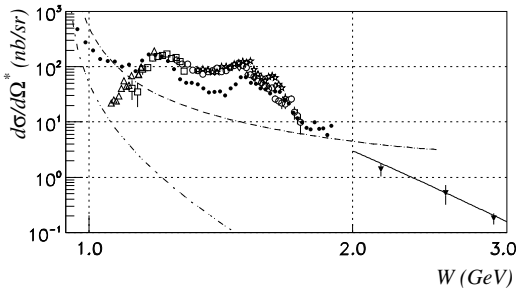

Figure 29: Comparison of $Q^2 = 1$ GeV^2 virtual compton scattering cross sections ($\bullet$) at $\theta_{\gamma\gamma}^{CM} = 167^\circ$ and real compton scattering data at $\theta_{\gamma\gamma}^{CM} = 159 - 160^\circ$ [34] ($\star$) $128 - 132^\circ$ [32] ($\diamond$), 141° [33] ($\triangle$), $130 - 132^\circ$ [35] ($\circ$), 131° [36] ($\Box$), $128 - 105^\circ$ [52] ($\times$). The solid curve is a s^{-6} scaling function normalized to the second Cornell point. The dashed curve is the Bethe-Heitler + Born cross section including the t-channel π^0 exchange diagram. The dotted curve is the Bethe-Heitler alone.

quarks–or baryon resonances) may become the essential degrees of freedom. In Fig. 29 we compare our virtual photo-absorption cross sections with the published data on large-angle real compton scattering. At large W the RCS and VCS cross sections are approximately equal. If the wide-angle RCS and VCS scattering amplitudes were dominated by resonance degrees of freedom, we would expect the VCS cross section in Fig. 29 to be over an order of magnitude less than the RCS cross section (roughly the square of the dipole form factor at $Q^2 = 1$ GeV^2). However, at large W the RCS and VCS cross sections are approximately equal. We consider this to be striking evidence that this back-angle VCS process is dominated by a single quark mechanism at large W and Q^2.

4.4 E97-103

Search for Higher Twist Effects in the Neutron Spin Structure Function $g_2^n(x, Q^2)$

T. Averett and W. Korsch, Spokespersons
K. Kramer, Ph.D. Student

Experiment E97-103 was successfully completed in the late summer of 2001. Spin asymmetries were measured using longitudinally polarized electrons scattered from either longitudinal or transversely polarized ^{3}He in the inclusive reaction $^3\vec{H}e(\vec{e}, e')$. From these measured asymmetries, the neutron spin structure function $g_2^n(x, Q^2)$ can be obtained. Data were collected at five values of Q^2 (0.58, 0.80, 0.96, 1.14, 1.36 GeV^2) at fixed $x \sim 0.2$, and with $W^2 > 4$ GeV^2. The two Hall A HRS spectrometers were used independently, with separate data acquisition systems, for detecting the scattered electrons. The Hall A polarized ^{3}He target was used and reached the highest average polarization (over 40%) ever achieved with $10 - 12$ μA of beam on target. The ^{3}He nuclei were polarized through spin-exchange collisions with optically-pumped, polarized rubidium atoms. The polarization direction could be oriented parallel or perpendicular to the beam line and three 30 W diode lasers (Coherent FAP systems) were used in each configuration for optical pumping. Target polarization was measured with using NMR and EPR systems.

By measuring both the parallel and perpendicular spin asymmetries, $A_\parallel$ and $A_\perp$, one can obtain the g_1 and g_2 structure functions. A correction is made to the ^{3}He results to obtain the structure functions for the neutron.

$$g_1(x, Q^2) = \frac{F_1(x, Q^2)}{D'} \left[A_\parallel + A_\perp \tan\theta/2 \right]$$

$$g_2(x, Q^2) = \frac{F_1(x, Q^2)}{D'} \frac{y}{2\sin\theta} \left[A_\perp \frac{E + E'\cos\theta}{E'} - A_\parallel \sin\theta \right]$$

$$D' = \frac{(1-\epsilon)(2-y)}{y(1+\epsilon R(x, Q^2))}$$

$$\epsilon = 1/(1 + 2(1 + \nu^2/Q^2)\tan^2\theta/2)$$

$$y = \nu/E$$

The g_1 structure function has been accurately measured at SLAC (deep-inelastic) and Jefferson Lab (E94-010, quasi-elastic and resonance regions) and is directly related to the spin decomposition of the nucleon in terms of quark flavors. For g_2 however, one must look beyond simple parton model interpretations. It is generally described in the framework of the Operator Product Expansion, where the hadronic matrix element which describes the physics of g_2 is expanded in a series of operators and unknown coefficients grouped according to their twist [37]. The twist describes the degree to which a term contributes to the matrix element, where terms with successively higher twist are suppressed by additional factors

of $1/\sqrt{Q^2}$. Leading twist (twist=2) describes the case where the virtual photon probes a single, non-interacting quark. This contribution is also the leading contribution to the g_1 structure function. The twist=3 contributions arise when the virtual photon interacts with a quark that is simultaneously exchanging a gluon with another quark. These twist=3 terms do not contribute to g_1, which means that a precise measurement of g_2 allows one to isolate and quantify the most basic quark-quark interactions within the nucleon.

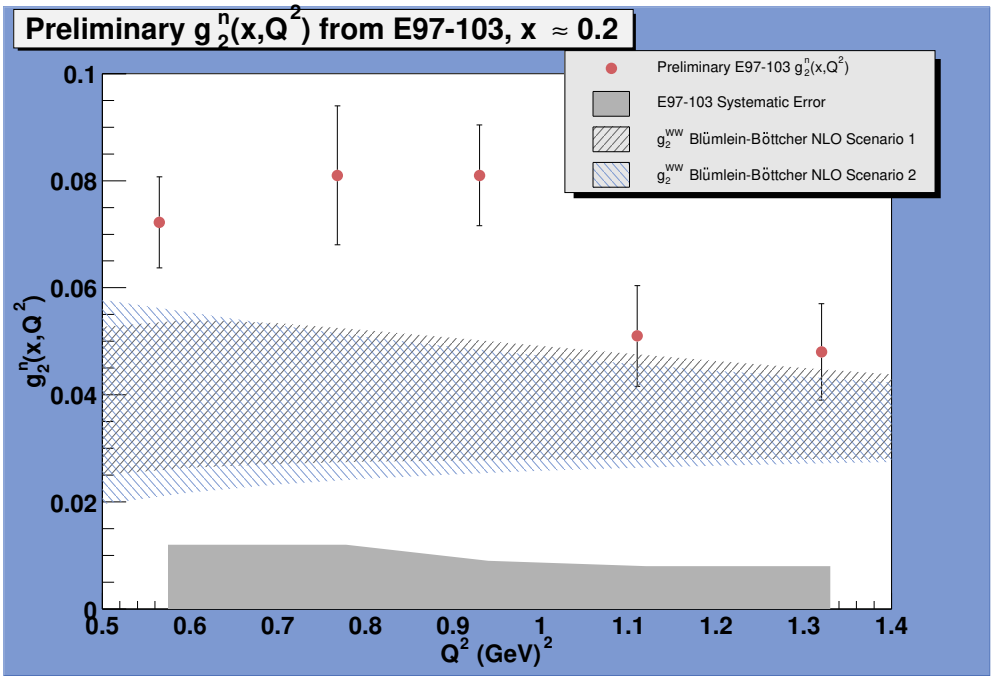

Figure 30: Preliminary results for g_2^n from E97-103. Errors are statistical with systematic errors shown by the solid band. Also shown are calculations of g_2^{ww} using the Blumlein and Bottcher NLO fit to world data on g_1.

Based on the Operator Product Expansion, Wandzura and Wilczek [38] derived the following expression for the twist=2 part of g_2:

$$g_2^{ww}(x,Q^2) = -g_1(x,Q^2) + \int_x^1 dy \frac{g_1(y,Q^2)}{y}$$

Thus, by measuring g_2 precisely and subtracting the leading g_2^{ww} contribution, one is left with only the twist=3 and higher contributions to g_2.

The raw asymmetries measured in this experiment were at the 10^{-3} to 10^{-4} level and great care was taken to ensure there were no significant false asymmetries. In particular, a third DAQ system based on the HAPPEX system was used to continuously monitor the beam charge asymmetry. This information was fed to the polarized source every ten minutes, where a feedback system was used to

zero the charge asymmetry with a rotatable half-wave plate at the source laser. Charge asymmetries were consistently kept well below the 50 ppm level. Data were also taken during the commissioning period using quasi-elastic scattering from thin carbon targets. The asymmetry from the carbon target was measured to be -67 ± 46 ppm in the left spectrometer, and -52 ± 44 in the right, which gives us confidence in our control of false asymmetries.

The data collected in E97-103 will allow us to calculate g_2^n at five values of Q^2, each with an absolute statistical error $< 10^{-2}$, which is an order of magnitude improvement over existing data from SLAC (Experiment E155x, preliminary results). Data analysis is now complete and a publication is being drafted for submission to PRL. Preliminary results for g_2^n are shown in Fig. 30 along with g_2^{ww} calculated using the Blumlein and Bottcher NLO fit [39] to world data. Results seem to indicate a systematic deviation fromg_2^{ww} as Q^2 decreases.

4.5 E97-110

The GDH Sum Rule, the Spin Structure of ^{3}He and the Neutron using Nearly Real Photons

J.-P. Chen, A. Deur, F. Garibaldi Spokespersons

The goal of the experiment is to measure the generalized Gerasimov-Drell-Hearn integral (GDH) at low Q^2 on the neutron and ^{3}He.

The GDH sum rule at $Q^2 = 0$ The GDH sum rule has been first derived at Q^2=0. For spin 1/2 targets it reads

$$\int_{\nu_0}^{\infty}(\sigma^{1/2} - \sigma^{3/2})\frac{d\nu}{\nu} = -2\pi^2\alpha\frac{\kappa^2}{M^2},$$

where $\sigma^{1/2}$ ($\sigma^{3/2}$) is the polarized photoproduction cross section when the photon helicity is anti-aligned (aligned) with the target spin. ν_0 is the pion photoproduction threshold, ν the photon energy, κ the anomalous magnetic moment of the target and M its mass.

The generalized GDH sum rule It has been suggested that the GDH *integral*, extended to finite Q^2, will help to understand the transition from perturbative to non-perturbative QCD. Recently Ji and Osborn derived a generalized GDH *sum rule* and showed that the Bjorken and the GDH sum rules are limiting cases of the generalized GDH sum rule. It is written

$$4\int_{\nu_0}^{\infty} G_{1(2)}\frac{d\nu}{v} = \overline{S_{1(2)}},$$

where $G_{1(2)}$ are the spin structure functions of the nucleon and $\overline{S_{1(2)}}$ are the forward Compton amplitudes with the elastic contribution subtracted. The forward Compton amplitudes are presently calculable using chiral perturbation theory at low Q^2 and Operator Product Expansion at larger Q^2. Eventually lattice QCD calculations will provide calculations at any Q^2. Data at intermediate Q^2 have already been taken in Hall A (exp. E94-010) [10]. The main goal of this experiment is to provide benchmark data on the neutron at low Q^2 to compare to χPT calculations. It is also important to check the GDH Sum Rule at the real photon point. We will do so by extrapolation from nearly real photon data. This will be the first verification of the original GDH sum rule on the neutron. We can also form the GDH sum rule on the ^{3}He nucleus. Studying this quantity brings information about the ^{3}He nuclear structure.

The experiment The experiment ran in April-May and July-August 2003. It was the first experiment to use a septum magnet. The left septum was not available. Without it the left HRS could not see the ^{3}He cell and was used as a

luminosity and beam false asymmetry monitor on a separate carbon target. Due to momentum range limitation on the right arm, it was not possible to gather the Q^2 points between 0.3 and 0.5 $(\mathrm{GeV/c})^2$ that would have overlapped with E94-010. We used the polarized beam and the polarized ^{3}He target to measure the inclusive $\overrightarrow{^3He}(\overrightarrow{e},e')X$ reaction. Both the asymmetry and cross section need to be extracted. The polarized target was modified to accommodate the small scattering angles, the insertion of the septum and the large septum field gradients. The beam energies ranged from 1.1 to 4.4 GeV, and the electrons were detected at 6^o and 9^o. The nucleus excitation spectrum was covered from quasi-elastic to the the resonances and beyond. The kinematical coverage is given in Fig. 31.

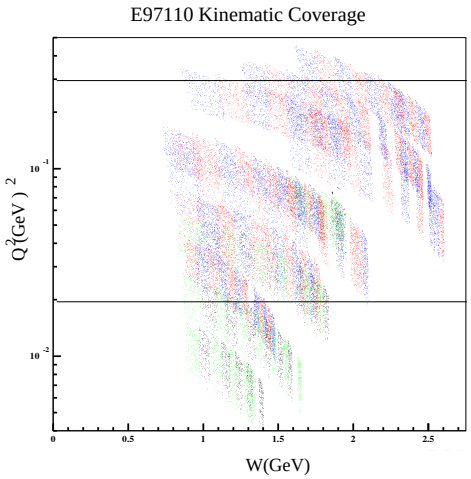

Figure 31: Kinematical coverage of the experiment.

The target polarization was about 40% average and the beam polarization was in general about 75%.

First run The first part of the experiment occurred in April-May 2003. During the commissioning the septum was found to be mis-wired. We decided to proceed with the low beam energy data taking because the 1.5 GeV data were critical for the experiment and it would have not been possible to reschedule it after the septum repair due to energy conflict with other halls. This option was possible because the large rates at 6^o were compensating for the significant acceptance loss. Indeed, the DAQ maximal rate was still the limiting factor. Consequently these data did not suffer loss in statistics. For each energy, we took systematic data to understand the optical properties of the spectrometer/septum combination. We also took systematic data for acceptance study and background subtraction. Consequently, we expect to extract cross sections at the 10% level. The online

analysis of the elastic data showed that the asymmetries are less sensitive to complications of having been taken with a mis-wired septum. The online results on the elastic asymmetries are plotted in Fig. 32.

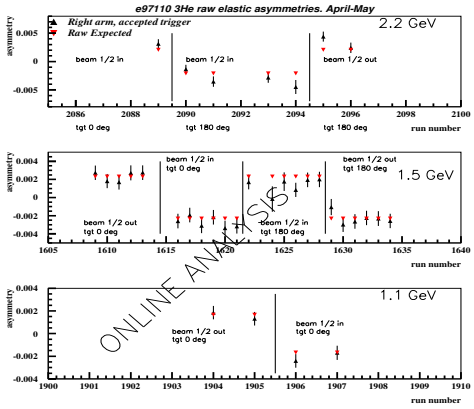

Figure 32: Elastic asymmetry online results for run 1.

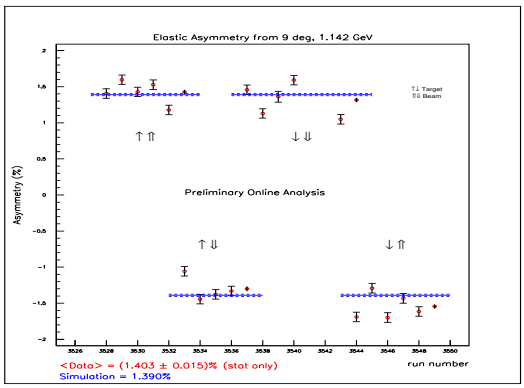

Figure 33: Elastic asymmetry online results for run 2.

During the first run we took the data requiring the newly designed target cell ("ice-cream cone cell"). This cell, by minimizing the rescattering background and radiative tails, allowed us to reach large enough W for a meaningful integration.

Second run The experiment was completed in July-August 2003. The septum was fixed in June and successfully commissioned. We completed 80% of our goal in term of statistics. The main loss of time was due to several CHL crashes. Online analysis showed a good data quality and good understanding of the background, see Fig. 33. The online elastic cross sections agree reasonably with the expectation.

Present state and outlook The spectrometer optics analysis for run 2 is close to completion. Optics data from run 2 are showed in Fig. 34.

The analysis under way comprises the detectors, the left arm/BCM data and the backgrounds. Transfer functions for the Septum/HRS are now available. The next steps are to carry out the optics and detector analyses for run 1, then proceed on to the analysis of the data for run 2. This analysis comprises target analysis (polarization, density), elastic analysis, acceptance study using carbon data, background study and simulation, extraction of the cross sections and asymmetries, radiative corrections and finally extraction of the physics quantities of interest: The extended GDH integral, the spin structure functions g_1 and g_2 and their moments. After the completion of the run 2 analysis, run 1 will be analyzed. Such a choice is driven by the fact that the run 1 data will be more delicate to analyze

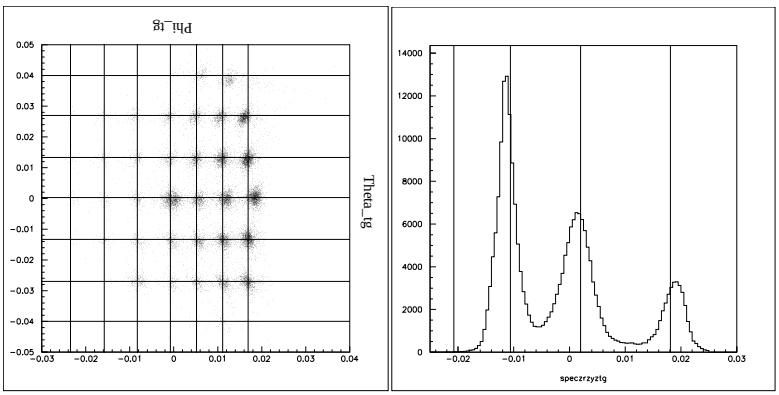

Figure 34: Optics data from run 2

and the run 2 analysis will provide valuable experience. The Q^2-position of the expected results with their uncertainty is given in the Fig. 35.

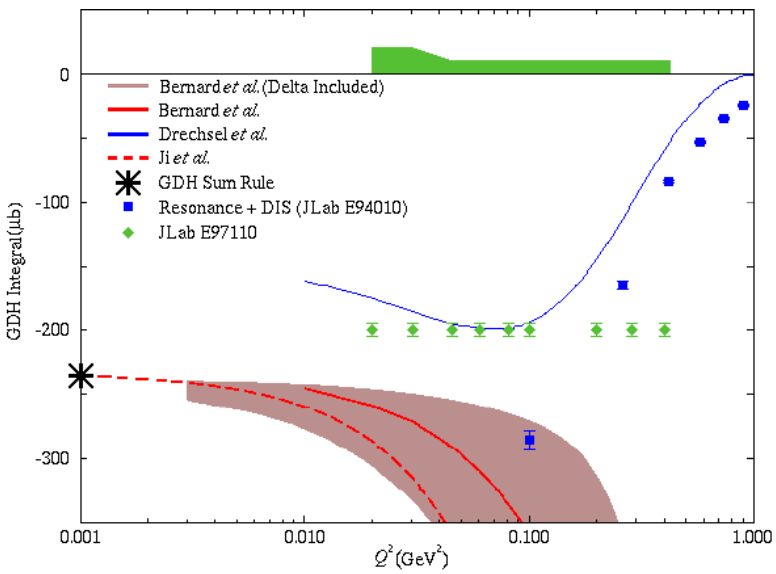

Figure 35: Q^2-position of the expected results with their uncertainty

4.6 E97-111

Systematic Probe of Short-Range Correlations via the Reaction $^4He(e,e'p)$

J. Mitchell, B. Reitz, and J. Templon, Spokespersons

Experiment E97-111 measured the unseparated cross section for the (e,e'p) reaction on ^{4}He at recoil momenta up to 530 MeV/c. In the plane-wave impulse approximation, many calculations predict a sharp minimum in the cross section for recoil momenta around 450 MeV/c and show that its location is sensitive to the short-range part of the internucleon potential. However, reaction dynamics effects such as final-state interactions (FSI) and meson-exchange currents (MEC) can obscure such a minimum. To distinguish and study these effects data were taken at several different kinematic points. Many ideas have been formulated about how to suppress contamination from these reaction dynamic processes in experiments. They can be partly avoided or at least minimized utilizing parallel kinematics, where the recoiled proton is detected along the q-axis. Therefore both $\vec{q}$ and $\vec{p}_s$ must line up to the final ejected-proton momentum and contaminating or multistep processes are suppressed. These qualitative arguments for utilizing parallel kinematics are also supported by calculations [40,41].

The beam energies available at JLab allow a substantial variation in the four momentum transfer Q^2 for a given (ϵ_m, p_m) region. Those variations are helpful in two respects: to help discriminate between one- and two-body currents contributing to the cross section and to suppress the contaminant two-body currents. The one-body direct knockout process of interest only depends on Q^2 through the electron-proton cross section σ_{ep}, while MEC and IC contributions are expected to have a very different Q^2 behavior. Higher values of Q^2 will help to suppress MEC and IC contributions due to the additional $1/Q^2$ dependences of the meson propagators $N\pi$ and $N\rho$, and of the $NN\pi$ ($NN\rho$) form factors.

Close to quasi-elastic kinematics the momentum transfer essentially determines the momentum of the outgoing proton. FSI are a strong function of the proton energy. From proton scattering experiments it is known that they are lowest at proton momenta of about 700 MeV/c. Above this momentum, absorption effects begin to increase, but the elastic rescattering continues to decrease. However, for the case of the two-body breakup the latter effect is more important; therefore higher momentum transfer appears to be favorable in terms of suppressing FSI.

The E97-111 experiment ran in the fall of 2000 using the standard equipment available in Hall A. The main emphasis was on measuring the ^{4}He(e,e'p)^{3}H cross section at recoil momenta up to 530 MeV/c in parallel kinematics at two different beam energies 2.389 GeV and 3.170 GeV/c. Additional data were taken in two quasi-perpendicular kinematics, with ω fixed to 525 and 487 MeV and Q^2 values of 1.78 and 1.82 (GeV/c)^2. The exclusiveness of the two-body breakup channel is guaranteed by means of cuts on the missing energy ϵ_m. The ^{4}He(e,e'p)^{3}H reaction will only occur at ϵ_m = 19.81MeV/c. The continuum is well separated, with a

threshold for the three-body breakup of 26.1 MeV and 28.3 MeV for the four-body breakup.

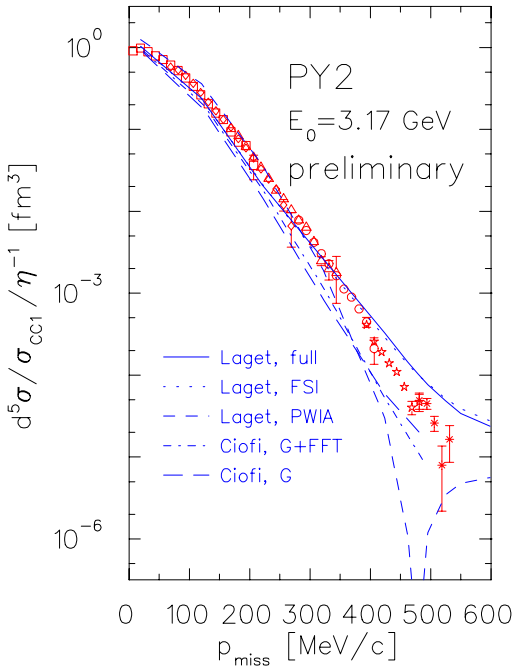

Figure 36: Preliminary results for the reduced cross sections at a beam energy of 3170 MeV. The error bars only show the statistical uncertainty. The dashed line (short dashes) shows the theoretical prediction by Laget in PWIA, the solid line depicts the full calculation, the dotted line only includes FSI. The dashed curve (long dashes) is a Glauber calculation by Ciofi and Morita, the dash-dotted curve additionally includes finite formation time effects.

Preliminary results for the reduced cross sections in the PY2 kinematics are shown in Fig. 36. The error bars show the statistical error only. The cross section is divided by the elementary e-p off-shell cross section σ_{CC1}, using the description of [42] and the recoil factor η, to remove the basic kinematical dependence on the polarization of the virtual photon. The reduced cross section falls monotonically within this momenta range. Two sets of theoretical predictions are shown. The first set from J.M. Laget [43] consists of a PWIA calculation (dashed), a calculation including FSI (dotted), and the full calculation (solid), including FSI as well as MEC and IC. For the FSI at lower energies the phase shift description of [44] was used, which describes elastic NN scattering. At higher energies the high energy parameterization of the NN scattering amplitude of [45] was used, its imaginary part representing the absorptive part of the NN interaction.

The second group of calculations is from H. Morita and C. Ciofi degli Atti

[46]. The first curve (long dashes) is a Glauber type calculation (labeled G), and the dashed-dotted curve (labeled G+FFT) additionally includes finite formation time (FFT) effects [47]. Although data were taken in parallel kinematics and at high momentum transfers, the reduced cross section still falls monotonically in the investigated region, with no sign of a minimum or a change in the slope. This feature appears in all but the PWIA calculations. Neither of the full calculations preserves the minimum in the spectral function at this kinematical setting. Laget's calculations indicate, that this is mainly due to FSI, whereas the inclusion of MEC and IC has only a small effect on the predicted cross section. These calculations also show that below 280 MeV/c the PWIA cross section is larger than the one of the full calculation, above that value the PWIA cross section is smaller. This indicates that the FSI tends to shift cross section from low p_m (where the spectral function is high) to the dip region (where the PWIA cross section is tiny). The FFT effects, which are believed to restore the minimum at very high momentum transfers, are in these kinematics not of great importance. At lower recoil momenta the full calculations of both groups give a reasonable description of the data. Starting at around 350 MeV/c they start to differ from the data and among themselves. Whereas the Laget calculation overpredicts the cross section, the Ciofi calculation underpredicts it at high missing momenta.

All production data of E97-111 have been replayed, as well as the runs for optics calibration, for the calibration of angular offsets, for target boiling studies, and for the ^{3}He(e,e) elastic reaction. To finalize the results further studies of detector efficiencies are ongoing. The elastic data need further anlysis to obtain the absolute normalization. Finally, a careful study of acceptance cuts and other systematic uncertainties is planned.

4.7 E98-108

Electroproduction of Kaons upto Q^2= 3 (GeV/c)^2

O.K. Baker, C.C. Chang, S. Frullani, M. Iodice and P. Markowitz,
Spokespersons
Contributed by P. Markowitz and M. Coman

The E98-108 collaboration [48] collected data initially in January, March and April 2001 and finished running in March 2002 (shown in Fig. 37 is the online missing mass spectra from the March 2002 kinematics).

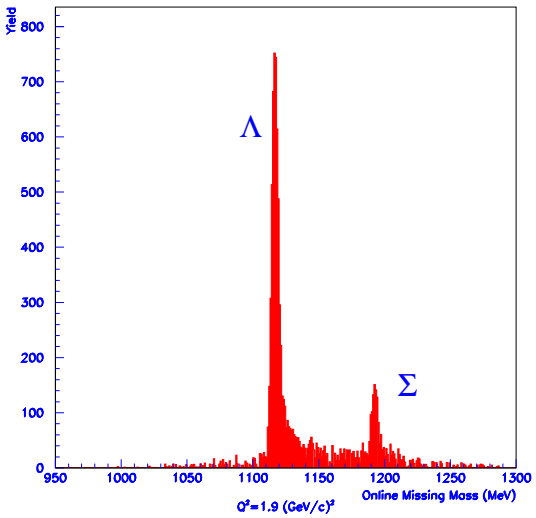

Figure 37: The online missing mass yield taken in March 2002 at Q^2 = 1.9 (GeV/c)^2, W = 1.95 GeV and $t = t_{min}$.

At a total of 30 kinematics points, the experiment measured the $H(e, e'K^+)Y$ cross section. Kinematics used momentum transfers of 1.90 and 2.35 (GeV/c)^2 and invariant masses between 1.8 and 2.2 GeV to measure the cross section as a function of ε (the photon longitudinal polarization), as well as measurements left and right of the direction of $\vec{q}$. Preliminary σ_L, σ_T, and σ_{LT} cross sections have been extracted from the data. The transverse cross section σ_T, and longitudinal-transverse interference cross section σ_{LT} is used to constrain the reaction mechanism. The behavior of the longitudinal cross section σ_L is mapped as a function of the Mandelstam variable t at fixed Q^2. The kaon form factor is expected to be senstivity to σ_L, albeit in a model-dependent way. The data will allow the kaon electroproduction reaction mechanism to be determined and eventually allow the kaon form factor to be modelled as well.

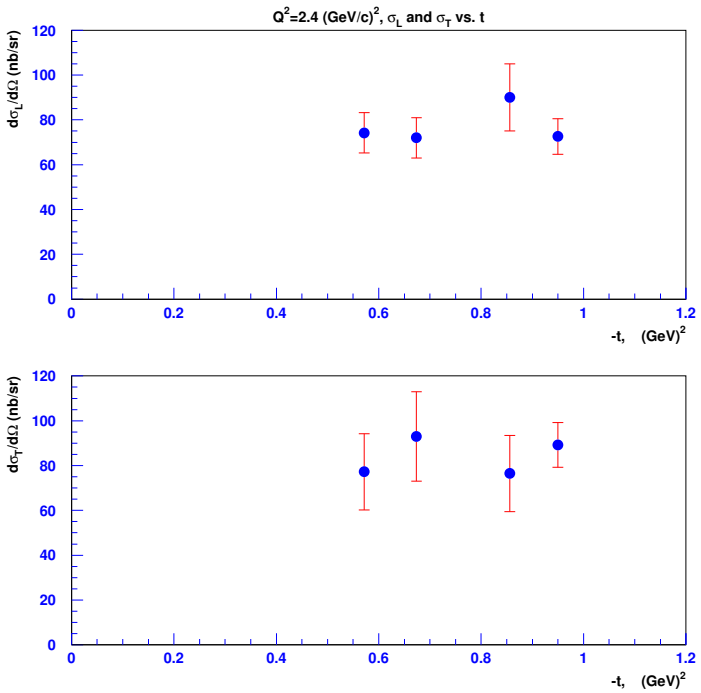

Figure 38: The longitudinal (upper) and transverse (lower) response function at Q^2- 2.35 GeV/c^2 for $H(e,e'K^+)$ as a function of the invariant 4-momentum, t.

The doctoral student analyzing the data (Marius Coman of Florida International University) is presently focussing on the systematic analysis (acceptance, normalizations, efficiencies and calibrations). For example, target "boiling" corrections are typically 4–6%, while VDC efficiency corrections (both for the detector firing all four planes and for reconstructing one unique track) typically total 20%. The wire chamber efficiency, electronic and computer deadtimes, and cut efficiencies have been determined. Radiative corrections have been done using the MCEEP simulation code; a comparison to the SIMC simulation code is underway.

The experiment required building two new aerogel Čerenkov radiation detectors with indices of refraction of 1.015 and 1.055. The first detector, due to the low index of refraction, required special handling of the delicate aerogel radiator. The first detector fired only on pions or lighter particles, but not on kaons or protons. The second aerogel was built primarily by the MIT group and fired on either kaons or protons but not pions. The use of two aerogels in anticoincidence is a novel PID idea. The response of the two new aerogels as a function of momenta has been studied in detail for protons, kaons and pions.

Preliminary separated longitudinal and transverse response function results as

a result of the invariant 4-momentum transfer t are shown in Fig. 38. The upper panel shows the Hall A data at Q^2=2.35 $(\mathrm{GeV/c})^2$ while the lower curve shows the transverse response fucntion. The error bars will decrease by a factor of 2–3 when the analysis is final.

The response functions were previously measured at lower Q^2 in Hall C by experiment E93-018. Plotted in Fig. 39 is the ratio of the longitudinal to the transverse response function from E93-018 and a point at the higher Q^2 of this experiment.

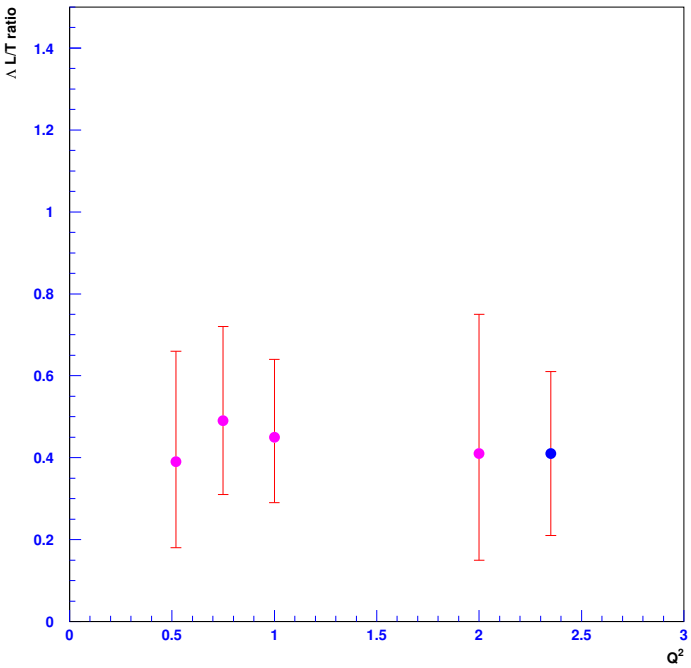

Figure 39: Shown are ratios of the longitudinal to transverse responses as a function of Q^2 from the previous E93-018 and from this experiment.

4.8 E99-114

Exclusive Compton Scattering on the Proton

C.E. Hyde-Wright, A. Nathan, B. Wojtsekhowski, Spokespersons

In the high energy limit, exclusive reaction cross sections are predicted to follow a scaling law[49]:

$$\frac{d\sigma}{dt} = s^{-n} f(\cos\theta^{CM}), \tag{5}$$

with $n = 6$ for real compton scattering (RCS). In Pertubative QCD, the $n = 6$ scaling law results from the exchange of two gluons amongst the three quarks of the lowest Fock state configuration in the proton wave function. However, in the handbag mechanism proposed in the energy regime of Jefferson Lab, only a single active quark couples to the incoming and outgoing photon via the Klein-Nishina process, while the soft components of the proton wave function absorb the momentum transfer to the single quark[50]. The handbag mechanism leads to predictions of fixed t scaling relations, and a new set of elastic form factors[51]

$$\begin{aligned} \frac{d\sigma}{dt} &= \frac{d\sigma^{KN}}{dt}\left\{\frac{1}{2}\left[R_V^2(t) + \tau R_T^2(t) + R_A^2(t)\right]\right. \\ &\qquad \left. - \frac{us}{s^2+u^2}\left[R_V^2(t) + \tau R_T^2(t) - R_A^2(t)\right]\right\} \qquad (6) \\ K_{LL} &= \frac{d\sigma^{KN}}{dt}\frac{s^2-u^2}{s^2+u^2} R_V(t) R_A(t), \qquad (7) \end{aligned}$$

where $d\sigma^{KN}$ is the Klein-Nishina cross section, and $\tau = -t/(4M^2)$. The RCS form factors are integrals of the large t Generalized Parton Distributions:

$$\begin{aligned} \int_{-1}^{1} \frac{dx}{x} \sum_f e_f^2 H_f(x,0,t) &= R_V(t) \\ \int \frac{dx}{|x|} \sum_f e_f^2 \tilde{H}_f(x,0,t) &= R_A(t) \qquad (8) \\ \int \frac{dx}{x} \sum_f e_f^2 E_f(x,0,t) &= R_T(t) \end{aligned}$$

The goals of the RCS experiment are to study the reaction mechanism and measure new form factors of the proton. This experiment is the subject of four Ph.D. theses: M. Roedelbronn (UIUC), D. Hamilton (Glasgow), A Danagulian (UIUC), and V. Mamyan (Yerevan). In Fig. 40 we present the preliminary cross section results. For each incident energy the plateau at maximum $-t$ is likely the result of non-perturbative u-channel Regge exchange. The preferred kinematic

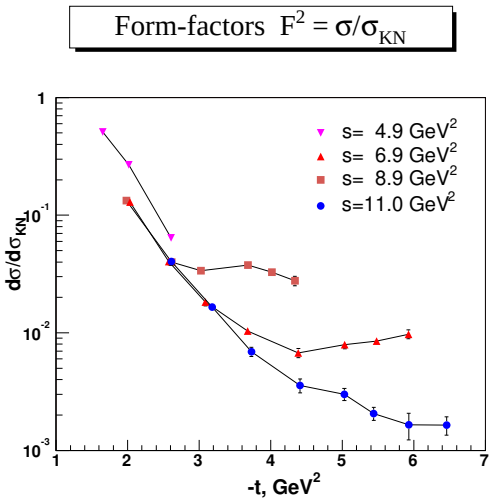

Figure 40: Preliminary $H(\gamma, \gamma p)$ cross sections, divided by the elementary Klein-Nishina cross section, as a function of the invariant momentum transfer t.

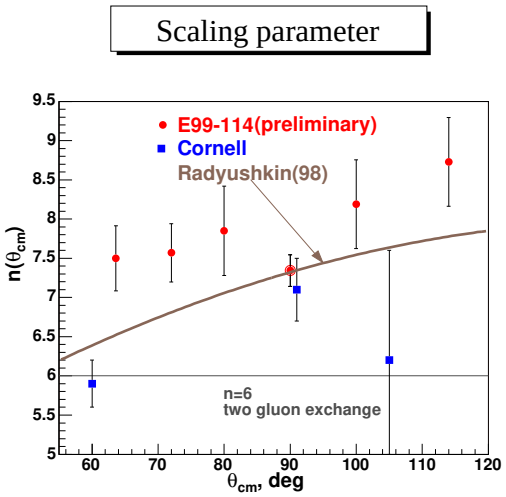

Figure 41: Preliminary fixed-angle scaling exponent (Eq. 5). The Cornell data are from [52]. The curve from A. Radyushkin is a prediction of the handbag hypothesis.

regime for evaluating the scaling behavior is for maximum $P_\perp$, at $\theta^{CM} = 90°$, or $-t \approx s/2$.

In Fig. 41 we display our preliminary results for the scaling exponent of Eq. 5 at fixed Center-of-Mass scattering angle. The new data are more consistent with the handbag mechanism than with the asymptotic pQCD scaling law of $n = 6$.

4.9 E00-007

Proton Polarization Angular Distribution in Deuteron Photo-Disintegration

R. Gilman, R. Holt, X. Jiang, Z.-E. Meziani, and K. Wijesooriya, Spokespersons

The experiment completed data taking in September-October 2002. The initial data taking consisted of about 10% (relative) calibrations of the focal plane polarimeter (FPP) analyzing power, at momenta of 2.4, 2.2, 2.0, and 1.7 GeV/c. These measurements used coincident ep scattering at 4.056 GeV beam energy. To improve the polarimeter performance, the left arm was configured as shown in Table 2, with two analyzers to improve the efficiency of detecting scattered particles. In this configuration, the front straw chambers determine both whether particles have scattered from the front analyzer, and the trajectory into the rear analyzer. By splitting the analyzer into two shorter halves, the inefficiencies that result from absorption of protons in a single thick analyzer are reduced.

Recoil polarization data were obtained at five center-of-mass angles, 37°, 53°, 70°, 90°, and 110°. Data for 110° were low enough in momentum to be taken with only the standard carbon FPP analyzer, obviating an ep calibration for this point. Estimated absolute statistical uncertainties on the polarization observables p_y, C_x, and C_z are in the range 0.05 - 0.10. At this point, the additional uncertainty from extra backgrounds from the target cells, related to the beam tuning and the cells being skewed relative to the beam, are not certain. Systematic uncertainties should be smaller than the statistical uncertainties.

Detector	**Function**
VDCs	tracking
S1	trigger
A1	π rejection
S0	trigger
CH_2	FPP front analyzer
straw chambers 1 and 2	FPP tracking
S2	-
Carbon	FPP rear analyzer
straw chambers 3 and 4	FPP tracking
π rejector / lead glass	-

Table 2: The left-arm detector stack used in the experiment.

Data taking is complete for E00-007, as the PAC approved beam time and goals of the experiment have been essentially obtained. The final analysis of the ep calibration and the γd data has not been completed at this time.

4.10 E00-102

Testing the Limits of the Single Particle Model in ^{16}O $(e, e'p)$

A. Saha, W. Bertozzi, L. B. Weinstein, and K. Fissum, Spokespersons
Contributed by R. Roché

Experiment E00-102 is an update to Hall A experiment E89-003: measurement of the cross section, R_{LT}, and A_{LT} for the ^{16}O $(e, e'p)$ reaction. Experiment E89-003 made measurements at energy and momentum transfer of $\varpi = 0.445$ GeV and $Q^2 = 0.8$ (GeV/c)^2, respectively, up to $p_{miss} = 0.345$ GeV/c [53–55]. This update experiment expands these measurements up to $p_{miss} = 0.755$ GeV/c at $\varpi = 0.449$ GeV and $Q^2 = 0.902$ (GeV/c)^2. The goals of these measurements are to determine:

- the limits of validity of the single-particle model of valence proton knockout;
- the effects of relativity and spinor distortion on valence proton knockout using the diffractive character of the A_{LT} asymmetry; and
- the bound-state wave function and spectroscopic factors for valence knockout.

The cross section will be determined for measurements from $p_{miss} = -0.515$ GeV/c to $p_{miss} = 0.755$ GeV/c, in order to determine the point at which single-knockout calculations fail and two-nucleon effects become important. R_{LT} and A_{LT} will be separated for p_{miss} up to ± 0.515 GeV/c to further test the relativistic DWIA calculations. Figure 42 shows anticipated data points from E00-102 for A_{LT} as a function of missing momentum for the $1p$-shell states along with data obtained from E89-003, both compared to calculations from Udias *et al.*

Data were taken at a fixed beam energy of 4.620 GeV/c, $\overrightarrow{q} = 1.066$ GeV/c, and $\theta_q = 56.22°$. Throughout the entire experiment, the electron arm (HRSl) was also fixed at 12.5° with a central momentum of 4.121 GeV/c, allowing it to be used as a luminosity monitor. The hadron arm (HRSr) angle varied from 28.3° to 96.1° to cover the necessary missing momentum range. These kinematics are shown in Fig. 43.

Both detector stacks were used in their standard configurations. Each stack, however, contained an additional S0 scintillator for checking trigger efficiency; and the HRSl contained a pion rejector to be used for addition particle identification of π^-'s. The target used was the Hall A self-normalizing three-foil waterfall target [56,57]. Each water foil was approximately 200 mg/cm^2 thick and separated by 25.4 mm at an angle of 57.4° with respect to the beam direction. Using the hydrogen in the water, precision calibrations can be made as well as normalization of cross sections to known ^{1}H $(e, e'p)$ and ^{1}H (e, e') cross sections.

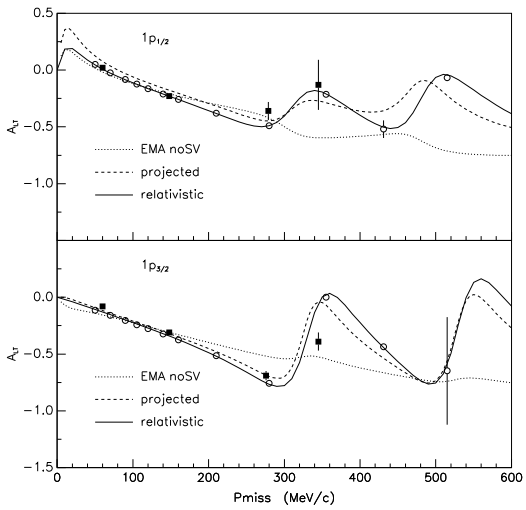

Figure 42: Projected A_{LT} data compared to E89-003 results and calculations of Udias *et al.* Open circles are anticipated data points from E00-102, solid squares are E89-003 data obtained at slightly different kinematics.

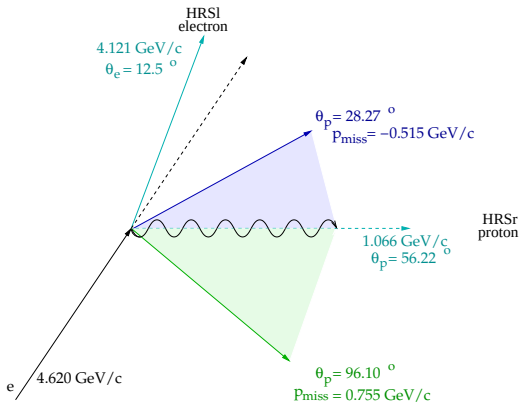

Figure 43: E00-102 kinematics. LHRS remained fixed at 12.5° throughout the experiment while RHRS varied around the direction of parallel kinematics.

In the past year, a change of post-docs working on data analysis has occurred. Header files have been corrected to include water foil target information. Spectrometer mispointing was rechecked using these new headers. Variables have now been added to the ntuple to calculate the electronic deadtime and VDC efficiencies run by run.

Data is currently being replayed using ESPACE. Hydrogen cross sections will be calculated very soon using parallel kinematics data. Once the entire replay

is complete oxygen cross sections, along with R_{LT} and A_{LT}, for each kinematic point will be calculated.

4.11 E01-001

New Measurement of (G_E/G_M) for the Proton

J. Arrington and R. E. Segel, Spokespersons

Experiments using the polarization transfer technique have reported [58,59] that in the $1 < Q^2 < 5.6$ GeV^2 range the ratio of proton electric to magnetic form factor falls off linearly with increasing Q^2, with the results well fit by $\mu_p G_E/G_M = (1 - 0.135(Q^2 - 0.24))$ [60]. Uncertainties in the individual points are 0.05 or less at moderate Q^2, and 0.10 or less for the larger Q^2 values. These results appear to contradict experiments going back as far as 1970 [61–67] using the Rosenbluth technique that are more in agreement with "scaling" ($\mu_p G_E/G_M \approx 1$). Global analyses of the Rosenbluth data also support this contention [60,65,68]. However, the error bars reported in the results from the individual Rosenbluth experiments are larger than those from the polarization transfer experiments, especially at high Q^2. The "Super Rosenbluth" experiment was undertaken with the goal of doing Rosenbluth separations with uncertainties in G_E/G_M comparable to those achieved with polarization transfer.

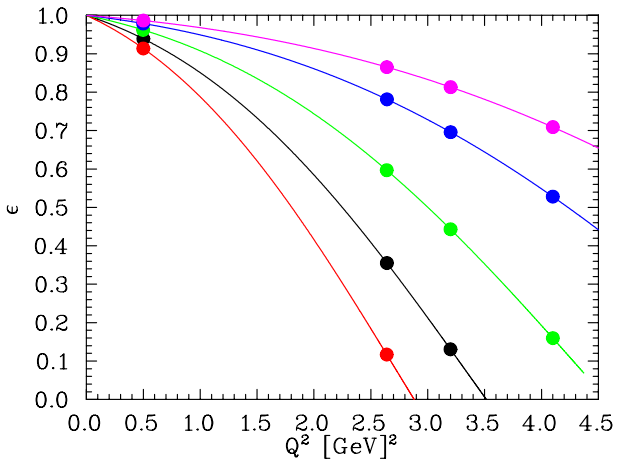

Figure 44: The (Q^2, ε) points at which proton spectra were taken. The lines are fixed values of beam energy: 1.912 (red), 2.262 (black), 2.842 (green), 3.772 (blue), and 4.702 GeV (magenta). The $Q^2 = 0.50$ GeV^2 points served to monitor the luminosity.

The experiment was run in May, 2002 using a 4 cm liquid hydrogen target and the HRS spectrometers. The separations were done with singles proton spectra. This is a departure from previous $p(e, e')p$ L-T separation experiments where electrons were detected. Detecting the protons has several important advantages [69]: (1) the momentum of the detected particles is independent of ε for a fixed Q^2

value, (2) the cross sections vary slowly as a function of ε, and (3) the radiative corrections are smaller than for electron detection. Separations were performed at three values of Q^2: 2.64, 3.20 and 4.10 GeV^2. Figure 44 shows the points at which data were taken. While the left HRS spectrometer was obtaining spectra at the Q^2 of interest, the right spectrometer was set at $Q^2 = 0.50$ GeV^2 and serving as a luminosity monitor [69]. At two kinematic settings, $p(e, e'p)$ coincidence spectra were taken with the right spectrometer detecting the electrons. These data are used to check efficiencies and spectral shapes.

The data have been replayed using the code ESPACE that generated ntuples that were passed on to a stand-alone analysis code, RECON. RECON calculates the angle and momentum for each event, applies cuts to reject events that scrape at the Q3 exit, and applies particle identification and kinematic cuts to identify protons in the region of the elastic peak. Corrections were applied for tracking inefficiency and dead time, which were no more than a few percent (except for computer dead time), and which are known to better than 0.5%.

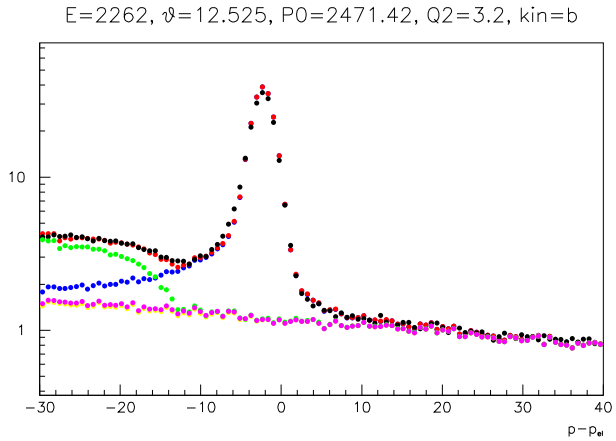

Figure 45: Missing momentum spectrum (in MeV) at $E_{beam} = 2.262$ GeV, $\theta_p = 12.526°$ ($Q^2 = 3.20$ GeV^2, $\varepsilon = 0.131$). The data from the LH2 target is shown in black, while the total simulated spectrum is in red. The spectrum is decomposed into contributions from the elastic peak (blue), protons from the $\gamma + p \to \pi^0 + p$ reaction (green) and protons coming from the solid endcaps of the target (magenta).

Figure 45 shows the missing momentum spectrum; measured proton momentum minus the momentum calculated from the measured scattering angle, assuming elastic scattering kinematics. The spectrum is dominated by the elastic peak but there are two backgrounds that have to be subtracted:

1. Reactions, primarily quasi-elastic scattering, in the endcaps of the target cell. This background was determined by taking data at every kinematic setting with

a dummy target.

2. Protons from the γ+p $\rightarrow \pi^0$+p reaction initiated by bremsstrahlung in the target's upstream endcap. These protons were significant only at forward angles and, because of the pion's finite mass, their spectrum cuts off below the elastic peak. Nevertheless, they had to be taken into account. Their contribution was modeled using a calculated bremsstrahlung spectrum and an s^{-7} cross section dependence, scaled to the measured background below the elastic peak. This background was insignificant at the $Q^2 = 0.50$ GeV^2 settings.

The elastic peak was modeled using the Monte Carlo code SIMC adopted to the HRS spectrometers. The code incorporates radiative corrections taken from the work of Mo and Tsai [71], with additional terms from [65] (the exact implementation is described in Ref. [70]). The breakdown of the spectrum into its three components is shown in Fig. 45. The $p(e,p)$ scattering cross sections were obtained from the normalization required to match the elastic peak calculated by the Monte Carlo code to that observed.

Preliminary results for the reduced cross sections, arbitrarily normalized to $\sigma_R \approx 1$, are shown as a function of ε for the three Q^2 values in Fig 46. The uncorrelated errors on the individual points are about 0.6%, and there is an additional systematic uncertainty on the ε-dependence (*i.e.* the Rosenbluth slope) of $\sim$0.6%. It is expected that further analysis will reduce these uncertainties. The current systematics are limited by the background subtraction and efficiency of the tracking cuts. Because we do not apply tight cuts on the 'quality' of the VDC information, we have a very high tracking efficiency, but long, non-gaussian tails in the reconstructed target quantities. Therefore, there is some uncertainty in the efficiency of the cut on the elastic peak, and we are forced to apply a very loose cut around the elastic peak to avoid losing too much of the data. We are working on improving the tracking, or else verifying that we can apply tight cuts on the track quality without introducing unacceptable uncertainties in the tracking efficiency. This will improve the uncertainty related to the tracking and the cuts, and will also allow us to use a tighter cut on the elastic peak, significantly reducing the size of the background corrections.

In the one-photon approximation the reduced cross section can be written $\sigma_R = \tau G_M^2 + \varepsilon G_E^2$, where ε is the polarization of the virtual photon. The slope of this linear function is proportional to $(G_E/G_M)^2$. Shown in Fig. 46 are the best fit to the present data using the form factor ratios obtained from a fit to all previous Rosenbluth data [60] and using those obtained in the polarization transfer measurements [58,59]. Clearly the present results are consistent with the previous Rosenbluth separation results and are not at all consistent with the polarization transfer determinations.

Accepting the E01-001 results leaves but two alternatives:

1. There is a flaw in the polarization transfer experiments or formalism. A continuation of the polarization transfer experiments in Hall C has been approved [72]

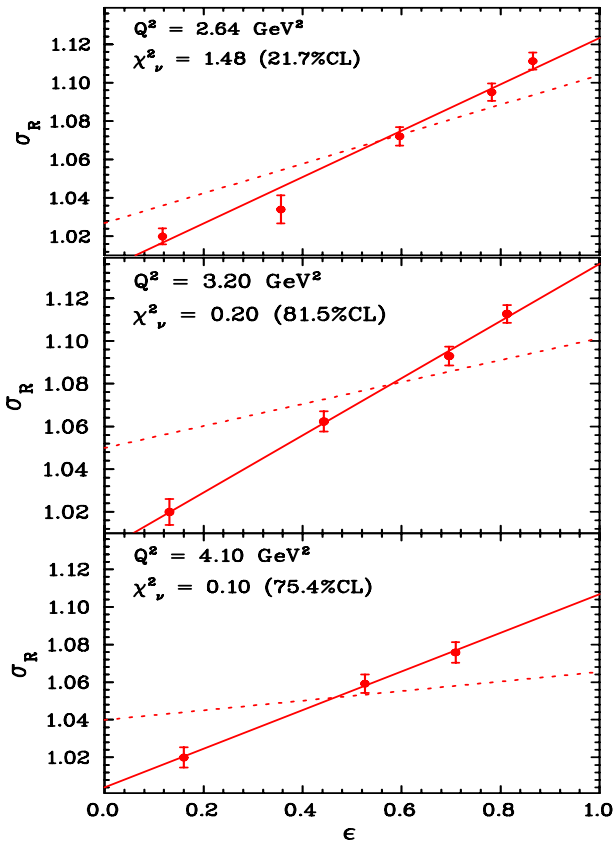

Figure 46: Reduced cross sections plotted as a function of ε. The solid line is the best linear fit to the data and the dotted line is the best fit with the slope fixed to match the results of the polarization transfer experiments [58,59].

and this will provide a check on the Hall A results. Also, a proposal to make an equivalent measurement of the form factor ratios using a polarized proton target [73], which was deferred pending the results of E01-001, may be revived now that the discrepancy has been confirmed.

2. The Rosenbluth data are not being interpreted correctly. The possibility that two-photon exchange corrections could explain the discrepancy is being intensively pursued and calculations [74–77] have shown that the contributions to the elastic cross section from this mechanism could be significant, and may have the potential to bring the two techniques into agreement. Considerable experimental and theoretical efforts are underway to determine if this is indeed the case.

5 References

[1] W. Bertozzi, E. Piasetzky, J. Waston, and S. Wood, spokespersons, Jefferson Lab Experiment E01-015, Studying the internal small-distance structure of Nuclei via the triple coincidence (e,e'p+N) measurement.

[2] J. Annand, D.W. Higinbotham, R. Lindgren, and V. Nelyubin, spokespersons, Jefferson Lab Experiment E01-014, Precision measurement of electroproduction of π^0 near threshold: a test of chiral QCD dynamics.

[3] G. Cates, K. McCormick, B. Reitz, B. Wojtsekhowski, spokespersons, Jefferson Lab Experiment E02-013, Measurement of the neutron electric form factor G_n^E at high Q^2.

[4] W. Bertozzi, B.E. Norum, T. Tamea, and K. Wang, spokespersons, Jefferson Lab Experiment E02-101, Exclusive study of deuteron electrodisintegration near threshold.

[5] W. Bertozzi, S. Gilad, D.W. Higinbotham, B.E. Norum, and S. Širca, spokespersons, Jefferson Lab Experiment E02-108, Measurement of A_x and A_z asymmetries in the quasi-elastic polarized ^{3}He($\vec{e}$,e'd) reaction.

[6] J.P. Chen, X. Jiang, and J.C. Peng, spokespersons, Jefferson Lab Experiment E03-004, Measurement of single target-spin asymmetry in semi-inclusive pion electroproduction on a transversely polarized ^{3}He target.

[7] E. Chudakov and V. Luppov, "Møller Polarimetry with Atomic Hydrogen Targets", Presented at IEEE 2003 Nuclear Science Symposium (NSS) in Portland, Oregon, 19-24 Oct 2003.

[8] S. Escoffier, "Mesure précise de la polarisation du faisceau d'électrons a TJNAF par polarimetrie Compton pour les expriences Gep et N-Delta", PhD thesis, CEA-Saclay.

[9] http://hallaweb.jlab.org/targets/polhe3/polhe3_tgt.html;
and tech notes in http://www.jlab.org/e94010/.

[10] M. Amarian *et al.*, Phys. Rev. Lett. 89, 242301 (2002); M. Amarian *et al.*, accepted by Phys. Rev. Lett., (2003), hep-ex/0310003.

[11] W. Xu *et al.*, Phys. Rev. Lett. 85, 2900 (2000); F. Xiong, *et al.*, Phys. Rev. Lett. 87, 242501 (2001).

[12] X. Zheng *et al.*, accepted for publication in Phys. Rev. Lett.

[13] JLab E97-103, spokespersons, T. Averett and W. Korsch;
http://hallaweb.jlab.org/physics/experiments/he3/g2/temp/

[14] JLab E01-012, spokespersons, J. P. Chen, S. Choi, N. Liyanage;
http://hallaweb.jlab.org/experiment/E01-012/

[15] JLab E97-110, spokespersons, J. P. Chen, A. Deur and F. Garibaldi;
http://hallaweb.jlab.org/experiment/E97-110/

[16] JLab E94-107, Spokespersons, S. Frullani, F. Garibaldi, J. LeRose, P. Markowitz, T. Saito.

[17] Alice Collaboration, *Technical Design Report of the High Momentum Particle Identification Detector*, CERN/LHCC98-19, Alice TDR 1, 14 August 1998.

[18] Hall A Report 2001.
[19] Hall A Report 2002.
[20] `http://hallaweb.jlab.org/root/`
[21] M. Rvachev, *Ph.D. Thesis*, Massachussetts Institute of Technology, Cambridge (2003).
[22] F. Benmokhtar, Proceedings of the $XVII^{th}$ *International IUPAP Conference on Few Body Problems in Physics*, Durham (North-Carolina, USA), June 5-10 (2003).
[23] J-M. LeGoff *et al.*, Phys. Rev. **C50** (1994) 2278.
[24] P. Ulmer *et al.*, Phys. Rev. Lett. **89** (2002) 062301.
[25] M. Mazzouz, *Diploma Dissertation*, Université Joseph Fourier, Grenoble (France) 2003.
[26] K. Joo *et al.*, Phys. Rev. Lett. **88**, 122001 (2002).
[27] D. Drechsel, O. Hanstein, S. S. Kamalov, L. Tiator, and S. N. Yang, www.kph.uni-mainz.de/MAID.
[28] S. S. Kamalov, S. N. Yang, D. Drechsel, O. Hanstein, and L. Tiator, Phys. Rev. **C 64**, 032201(R) (2001).
[29] R. A. Arndt, W. J. Briscoe, R. L. Workman, and I. I. Strakovsky, gwdac.phys.gwu.edu.
[30] P. A. Guichon, G. Q. Liu and A. W. Thomas, Nucl. Phys. **A591**, 606 (1995).
[31] B. Pasquini, *et al.* Eur. Phys. J. A **11**, 185 (2001) [arXiv:hep-ph/0102335].
[32] M. Jung, *et al.* Z. Phys. C **10**, 197 (1981).
[33] E. L. Hallin *et al.*, Phys. Rev. C **48**, 1497 (1993).
[34] Y. Wada *et al.*, Nucl. Phys. B **247**, 313 (1984).
[35] T. Ishii *et al.*, Nucl. Phys. B **254**, 458 (1985).
[36] F. Wissmann *et al.*, Nucl. Phys. A **660**, 232 (1999).
[37] R.L. Jaffe and X. Ji, Phys. Rev. **D43**, 724 (1991).
[38] S. Wandzura and F. Wilczek, Phys. Lett. **B72**, 195 (1977).
[39] J. Blumlein and H. Bottcher, Nuc. Phys. **B636**, 225 (2002).
[40] A. Bianconi and M. Radici, Phys. Lett. B **363**, 24 (1995).
[41] L.L. Frankfurt, M.M. Sargsian, and M.I. Strikman, Phys. Rev. C **56**, 1124 (1997).
[42] T. deForest, Jr., Nucl. Phys. **A392**, 232 (1983).
[43] J.M. Laget, private communication.
[44] J.M. Laget, Nucl. Phys. **A579**, 333 (1994).
[45] J.M. Laget, nucl-th/0303052 (2003).
[46] C. Ciofi degli Atti and H. Morita, private communication.
[47] H. Morita, M.A. Braun, C. Ciofi degli Atti, and D. Treleani, Nucl. Phys. **A699**, 328c (2002).
[48] http://www.jlab.org/markowit/index.html
[49] S.J. Brodsky, and G. Farrar, Phys. Rev. Lett. **31**, 1953 (1973)
[50] A.V. Radyushkin, Phys. Rev., **D58**, 114008 (1998).
[51] H.W. Huang, P. Kroll, T. Morii, Eur. Phys. J. **C23**, 301 (2002).

[52] M. A. Shupe *et al.*, Phys. Rev. D **19**, 1921 (1979).
[53] A. Saha, contact person, Study of the Quasi Elastic $(e, e'p)$ Reaction in ^{16}O at High Recoil Momentum, JLab experiment E89-003.
[54] J. Gao *et al.*, Phys. Rev. Lett. **84**, 3265 (2000).
[55] N. Liyanage *et al.*, Phys. Rev. Lett. **86**, 5670 (2001).
[56] F. Garibaldi *et al.*, Nucl. Instr. Meth. in Phys. Res. **A314**, 1 (1992).
[57] E. Cisbani *et al.*, *A Waterfall Target System for Hall A at Jefferson Lab*, INFN/ISS **97/04** (1997).
[58] M. K. Jones *et al.*, Phys. Rev. Lett. **84**, 1398 (2000).
[59] O. Gayou *et al.*, Phys. Rev. Lett. **88**, 092301 (2002).
[60] J. Arrington, Phys. Rev. C **68**, 034325 (2003).
[61] J. Litt *et al.*, Phys. Lett. B **31**, 40 (1970).
[62] Ch. Berger *et al.*, Phys. Lett. B **35**, 87 (1971).
[63] L. E. Price *et al.*, Phys. Rev. D **4**, 45 (1971).
[64] W. Bartel *et al.*, Nucl. Phys. **B58**, 429 (1971).
[65] R. C. Walker *et al.*, Phys. Rev. D **49**, 5671 (1994).
[66] L. Andivahis *et al.*, Phys. Rev. D **50**, 5491 (1994).
[67] M. E. Christy, to be submitted to Phys. Rev. C.
[68] P. E. Bosted *et al.*, Phys. Rev. C **51**, 409 (1995).
[69] R. E. Segel, J. Arrington *et al.*, proposal E01-001.
[70] R. Ent *et al.*, Phys. Rev. C **64**, 054610 (2001).
[71] L. W. Mo and Y. S. Tsai, Rev. Mod. Phys. 41. 205 (1969).
[72] C. F. Perdrisat *et al.*, proposal E01-109.
[73] G. Warren *et al.*, proposal PR01-105.
[74] P. A. M. Guichon and M. Vanderhagen, Phys. Rev. Lett. **91**, 142303 (2003).
[75] P. G. Blunden, W. Melnitchouk and J. A. Tjon, Phys. Rev. Lett. **91**, 142304 (2003).
[76] A. Afanasev, Workshop on Nucleon Form Factors & Parity Violation, Athens, (2003) and private communication.
[77] M. P. Rekalo and E. Tomasi-Gustafsson, nucl-th/0307066

6 Hall A Collaboration Member List

Bryon Anderson	*Kent State University*
Mattias Andersson	*University of Lund*
Konrad A. Aniol	*California State University*
John Annand	*University of Glasgow*
David S. Armstrong	*College of William and Mary*
John Arrington	*Argonne National Laboratory*
Todd Averett	*College of William and Mary*
Maud Baylac	*Jefferson Laboratory*
Elizabeth Beise	*University of Maryland*
Fatiha Benmokhtar	*Rutgers, The State University of New Jersey*
Jacques Berthot	*Université Blaise Pascal, Clermont-Ferrand*
Pierre Bertin	*Université Blaise Pascal, Clermont-Ferrand*
Bill Bertozzi	*Massachusetts Institute of Technology*
Louis Bimbot	*Institut de Physique Nucléaire, Orsay*
Tim Black	*Massachusetts Institute of Technology*
Werner Boeglin	*Florida International University*
Alexander Borissov	*University of Glasgow*
Ed Brash	*University of Regina*
Vincent Breton	*Université Blaise Pascal, Clermont-Ferrand*
Herbert Breuer	*University of Maryland*
Etienne Burtin	*DAPNIA/SPhN, CEA, Saclay*
John Calarco	*University of New Hampshire*
Alexandre Camsonne	*Université Blaise Pascal, Clermont-Ferrand*
Larry Cardman	*Jefferson Laboratory*
Gordon D. Cates	*University of Virginia*
Christian Cavata	*DAPNIA/SPhN, CEA, Saclay*
Zengwei Chai	*Massachusetts Institute of Technology*
George Chang	*University of Maryland*
Ting Chang	*University of Illinois*
Nicholas Chant	*University of Maryland*
Jian-Ping Chen	*Jefferson Laboratory*
Seonho Choi	*Temple University*
Eugene Chudakov	*Jefferson Laboratory*
Steve Churchwell	*Duke University*
Evaristo Cisbani	*INFN/Sezione Sanità*
Leon Cole	*Hampton University*
Marius Coman	*Florida International University*
Benjamin Crowe	*North Carolina Central University*

Francesco Cusanno	*INFN/Sezione Sanità*
Dan Dale	*University of Kentucky*
Areg Danagoulian	*University of Illinois*
Nathalie Degrande	*Gent State University*
Raffaele De Leo	*INFN/Sezione Bari*
Alexandre Deur	*University of Virginia*
Nicole d'Hose	*DAPNIA/SPhN, CEA, Saclay*
Sonja Dieterich	*Rutgers, The State University of New Jersey*
Rachele di Salvo	*INFN/Sezione Roma2*
Pibero Djawotho	*College of William and Mary*
Frank Dohrmann	*Argonne National Laboratory*
Jean-Eric Ducret	*DAPNIA/SPhN, CEA, Saclay*
Dipangkar Dutta	*Massachusetts Institute of Technology*
Kim Egiyan	*Yerevan Physics Institute*
Martin B. Epstein	*California State University*
Stephanie Escoffier	*DAPNIA/SPhN, CEA, Saclay*
Robert Feuerbach	*Jefferson Lab*
Mike Finn	*College of William and Mary*
Kevin Fissum	*University of Lund*
Helene Fonvieille	*Université Blaise Pascal, Clermont-Ferrand*
Bernard Frois	*DAPNIA/SPhN, CEA, Saclay*
Salvatore Frullani	*INFN/Sezione Sanità*
Haiyan Gao	*Duke University*
Franco Garibaldi	*INFN/Sezione Sanità*
Ashot Gasparian	*Hampton University*
Olivier Gayou	*Massachusetts Institute of Technology*
Shalev Gilad	*Massachusetts Institute of Technology*
Ron Gilman	*Rutgers, The State University of New Jersey*
Alexander Glamazdin	*Kharkov Institute of Physics and Technology*
Charles Glashausser	*Rutgers, The State University of New Jersey*
Javier Gomez	*Jefferson Laboratory*
Victor Gorbenko	*Kharkov Institute of Physics and Technology*
Tim Gorringe	*University of Kentucky*
Keith Griffioen	*College of William and Mary*
David Hamilton	*University of Glasgow*
Ole Hansen	*Jefferson Laboratory*
David Hayes	*Old Dominion University*
Bill Hersman	*University of New Hampshire*
Doug Higinbotham	*Jefferson Laboratory*
Wendy Hinton	*Old Dominion University*
Richard Holmes	*Syracuse University*
Harry Holmgren	*University of Maryland*

Maurik Holtrop	*University of New Hampshire*
Edik Hovhannisyan	*Yerevan Physics Institute*
Calvin Howell	*Duke University*
Garth Huber	*University of Regina*
Charles Hyde-Wright	*Old Dominion University*
Hassan Ibrahim	*Old Dominion University*
Ru Igarashi	*University of Saskatchewan*
Sebastian Incerti	*Temple University*
Mauro Iodice	*INFN/Sezione Sanità*
Riccardo Iommi	*INFN/Sezione Sanità*
Dave Ireland	*University of Glasgow*
Kees de Jager	*Jefferson Laboratory*
Stephanie Jaminion	*Université Blaise Pascal, Clermont-Ferrand*
Steffen Jensen	*California Institute of Technology*
Xiaodong Jiang	*Rutgers, The State University of New Jersey*
Cathleen Jones	*California Institute of Technology*
Mark K. Jones	*Jefferson Laboratory*
Seigo Kato	*Yamagata University*
Mina Katramatou	*Kent State University*
Lisa Kaufman	*University of Massachusetts*
James Kellie	*University of Glasgow*
James Kelly	*University of Maryland*
Sophie Kerhoas	*DAPNIA/SPhN, CEA, Saclay*
Armen Ketikyan	*Yerevan Physics Institute*
Kouichi Kino	*Tohoku University*
Norm Kolb	*University of Saskatchewan*
Ioannis Kominis	*Princeton University*
Wolfgang Korsch	*University of Kentucky*
Serge Kox	*Institut des Sciences Nucléaires, Grenoble*
Alexander Kozlov	*University of Regina*
Kevin Kramer	*College of William and Mary*
Laird Kramer	*Florida International University*
Krishna S. Kumar	*University of Massachusetts*
Gerfried Kumbartzki	*Rutgers, The State University of New Jersey*
Geraud Lavessiere	*Université Blaise Pascal, Clermont-Ferrand*
John LeRose	*Jefferson Laboratory*
Mark Leuschner	*University of New Hampshire*
David Lhuillier	*DAPNIA/SPhN, CEA, Saclay*
Richard Lindgren	*University of Virginia*
Ken Livingston	*University of Glasgow*
Nilanga Liyanage	*University of Virginia*
George Lolos	*University of Regina*

Robert Lourie	*Renaissance Technology*
Bin Ma	*Massachusetts Institute of Technology*
Richard Madey	*Kent State University*
Kazushige Maeda	*Tohoku University*
Vahe Mamyan	*Yerevan Physics Institute*
Mark Manley	*Kent State University*
Demetrius Margaziotis	*California State University*
Pete Markowitz	*Florida International University*
Jacques Marroncle	*DAPNIA/SPhN, CEA, Saclay*
Jacques Martino	*SUBATECH, IN2P3, Nantes*
Samvel Mayilyan	*Yerevan Physics Institute*
Kathy McCormick	*Rutgers, The State University of New Jersey*
David Meekins	*Jefferson Laboratory*
Zein-Eddine Meziani	*Temple University*
Bob Michaels	*Jefferson Laboratory*
Brian Milbrath	*Eastern Kentucky University*
Wilson Miller	*University of Virginia*
Joseph Mitchell	*Renaissance Technology*
Bryan Moffit	*College of William and Mary*
Peter Monaghan	*Massachusetts Institute of Technology*
Jean Mougey	*Institut des Sciences Nucléaires, Grenoble*
Pierre Moussiegt	*ISN Grenoble*
Carlos Munoz-Camacho	*DAPNIA/SPhN, CEA, Saclay*
Sirish Nanda	*Jefferson Laboratory*
Alan Nathan	*University of Illinois*
Vladimir Nelyubin	*Gatchina*
Damien Neyret	*DAPNIA/SPhN, CEA, Saclay*
Dima Nikolenko	*Budker Institute of Nuclear Physics*
Blaine Norum	*University of Virginia*
Zisis Papandreou	*University of Regina*
Kent Paschke	*University of Massachusetts*
Emilie Penel-Notarris	*Institut des Sciences Nucléaires, Grenoble*
J.C. Peng	*University of Illinois*
Lubomir Penchev	*College of William and Mary*
Charles Perdrisat	*College of William and Mary*
Gerassimos G. Petratos	*Kent State University*
Artush Petrosyan	*Yerevan Physics Institute*
Eli Piasezky	*Tel Aviv University*
Stephane Platchkov	*DAPNIA/SPhN, CEA, Saclay*
Roman Pomatsalyuk	*Kharkov Institute of Physics and Technology*
Dan Protopopescu	*University of Glasgow*
Vina Punjabi	*Norfolk State University*
Thierry Pussieux	*DAPNIA/SPhN, CEA, Saclay*

Issam Qattan	*North-Western University*
Gilles Quéméner	*Institut des Sciences Nucléaires, Grenoble*
Igor Rachek	*Budker Institute of Nuclear Physics*
Ronald Ransome	*Rutgers, The State University of New Jersey*
Brian Raue	*Florida International University*
Juerg Reinhold	*Florida International University*
Bodo Reitz	*Jefferson Laboratory*
Yves Roblin	*Jefferson Laboratory*
Rikki Roché	*Florida State University*
Mike Roedelbronn	*University of Illinois*
Oscar Rondon	*University of Virginia*
Guenther Rosner	*University of Glasgow*
David Rowntree	*Massachusetts Institute of Technology*
Gary Rutledge	*TRIUMF*
Marat Rvachev	*Massachusetts Institute of Technology*
Franck Sabatie	*DAPNIA/SPhN, CEA, Saclay*
Arun Saha	*Jefferson Laboratory*
Teijiro Saito	*Tohoku University*
Adam J. Sarty	*Saint Mary's University*
Ralph Segel	*Northwestern University*
Andrei Semenov	*Kent State University*
Albert Shahinyan	*Yerevan Physics Institute*
Simon Sirca	*Massachusetts Institute of Technology*
Karl Slifer	*Temple University*
Timothy Smith	*University of New Hampshire*
Patricia Solvignon	*Temple University*
Pavel Sorokin	*Kharkov State University*
Paul A. Souder	*Syracuse University*
Steffen Strauch	*George Washington University*
Riad Suleiman	*Massachusetts Institute of Technology*
Vincent Sulkovsky	*College of William and Mary*
Jeff Templon	*NIKHEF*
Tatsuo Terasawa	*Tohoku University*
Luminita Todor	*Carnegie Mellon University*
H. Tsubota	*Tohoku University*
Hiroaki Ueno	*Yamagata University*
Paul E. Ulmer	*Old Dominion University*
Guido Urciuoli	*NFN/Sezione Sanità*
Antonin Vacheret	*DAPNIA/SPhN, CEA, Saclay*
Luc Van de Hoorebeke	*Gent State University*
Robert Van de Vyver	*Gent State University*

Pascal Vernin	*DAPNIA/SPhN, CEA, Saclay*
Branislav Vlahovic	*North Carolina Central University*
Hakob Voskanyan	*Yerevan Physics Institute*
Eric Voutier	*Institut des Sciences Nucléaires, Grenoble*
Richard Walter	*Duke University*
Kebin Wang	*University of Virginia*
John Watson	*Kent State University*
Dan Watts	*University of Glasgow*
Larry Weinstein	*Old Dominion University*
Richard Wilson	*Harvard University*
Krishni Wijesooriya	*Argonne National Laboratory*
Bogdan Wojtsekhowski	*Jefferson Laboratory*
Hong Xiang	*Massachusetts Institute of Technology*
Feng Xiong	*Massachusetts Institute of Technology*
Wang Xu	*Massachusetts Institute of Technology*
Jianguo Zhao	*General Electric*
Xiaochao Zheng	*Massachusetts Institute of Technology*
Zilu Zhou	*Massachusetts Institute of Technology*
Jindong Zhu	*Massachusetts Institute of Technology*
Lingyan Zhu	*Massachusetts Institute of Technology*
Xiaofeng Zhu	*College of William and Mary*
Piotr Zolnierczuk	*University of Kentucky*

7 Publications

- "Polarization Transfer in the $^4He(\vec{e},e'\vec{p})^3H$ Reaction up to $Q^2 = 2.6$ (GeV/c)^2", S. Strauch *et al.*, Phys. Rev. Lett. **91**, 052301 (2003).
- "Nuclear Transparency with the $\gamma n \to \pi^- p$ Process in ^{4}He", D. Dutta *et al.*, Phys. Rev. C **68**, 021001(R) (2003).
- "Cross-Section Measurement of Charged-Pion Photoproduction from Hydrogen and Deuterium", L.Y. Zhu *et al.* (The Jefferson Lab Hall A Collaboration), Phys. Rev. Lett. **91**, 022003 (2003).
- "Plane-wave Impulse Approximation Extraction of the Neutron Magnetic Form Factor from Quasielastic $^3\vec{H}e(\vec{e},e')$ at $Q^2 = 0.3$ to 0.6 (GeV/c)^2", W. Xu *et al.*, Phys. Rev. C **67**, 012201 (2003).

- "Precision Measurement of the Neutron Spin Asymmetry A_1^n and spin-flavor Decomposition in the Valence Quark Region.", X. Zheng *et al.*, Accepted by Phys. Rev. Lett.
- "Q^2 Evolution of the Neutron Spin Structure Moments Using a ^{3}He Target.", M. Amarian *et al.*, Accepted by Phys. Rev. Lett.
- "Basic Instrumentation for Hall A at Jefferson Jab", J. Alcorn *et al.*, Accepted by Nucl. Instr. Meth.

8 Theses

i. Precision Measurement of Neutron Spin Asymmetry A_1^n at Large x_{bj} using CEBAF at 5.7 GeV
Xiaochao Zheng, Massachusetts Institute of Technology, Dec. 2002

ii. Measurement of Polarization Observables in the Electro-Excitation of the Proton to its First Excited State
Rikki Roché, Florida State University, Aug. 2003

iii. Study of the N to $Delta$ Transition via $p(e,e'p)\pi_0$ Reaction
Zhengwei Chai, Massachusetts Institute of Technology, Aug. 2003

iv. A Search for Higher Twist Effects in the Spin Structure Function $g_2^n(x,Q^2)$
Kevin Kramer, College of William and Mary, Aug. 2003

v. Study of the Quasielastic $^3He(e,e'p)$ Reaction at $Q^2 = 1.5$ (GeV/c)^2 up to Missing Momenta of 1 GeV/c
Marat Rvachev, Massachusetts Institute of Technology, Sept. 2003

vi. Exclusive Photoproduction of Charged Pions in Hydrogen and Deuterium from 1 to 6 GeV
Lingyan Zhu, Massachusetts Institute of Technology, Dec. 2003